Electron Scattering Studies of Calcium and Titanium Isotopes*

R. F. Frosch,† R. Hofstadter, J. S. McCarthy, G. K. Nöldeke,‡ K. J. van Oostrum,§ and M. R. Yearian
Department of Physics and High Energy Physics Laboratory, Stanford University, Stanford, California 94305

AND

B. C. Clark and R. Herman
Research Laboratories, General Motors Corporation, Warren, Michigan 48090

AND

D. G. Ravenhall
Department of Physics, University of Illinois, Urbana, Illinois 61801

(Received 20 May 1968)

Experimental results are presented on the scattering of 250-MeV electrons by Ca^{40}, Ca^{42}, Ca^{44}, Ca^{48}, and Ti^{48}, and of 500-MeV electrons by Ca^{40} and Ca^{48}. An analysis is made in terms of a phenomenological three-parameter shape, and a new, more accurate charge distribution is obtained for Ca^{40}. The experiments also lead to a detailed exploration of the radial dependence of the differences in charge distributions of the various isotopes. Implications for nuclear theory are discussed. Comparison is made with the results of other electron scattering and of muonic x-ray experiments. The latter comparison permits an independent determination of an upper limit on the muon electromagnetic radius $\langle r^2\rangle_\mu^{1/2} \lesssim 0.35$ F.

I. INTRODUCTION

THE nuclear charge distribution of Ca^{40} obtained by elastic electron scattering has been the object of several investigations based on experiments performed at Stanford.[1–3] Hahn, Ravenhall, and Hofstadter[1] measured the relative values of the differential cross section at 183 MeV, and analyzed them to obtain a charge distribution. The Fermi shape used was found to have a half-radius and a skin thickness whose values were in accord with those of a range of nuclei examined. Crannell *et al.*,[2] by making a comparison with hydrogen cross sections, calibrated the Ca^{40} cross section on an absolute scale. The data of Ref. 1 were reexamined in greater detail by Ravenhall, Herman, and Clark,[4] who also made a comparison with muonic x-ray energy measurements. Other shapes besides the Fermi shape were examined, and the consistency, to within the experimental error, of the charge distributions obtained from muonic x rays and from electron scattering was established. Elastic scattering at a higher energy, 250 MeV, was performed by Croissiaux *et al.*[3] The increased experimental accuracy, and extended range of recoil momenta, narrowed the range of permitted shapes to something in between a "Fermi" and a "modified Gaussian," and produced considerably more precise radius and skin-thickness values for these shapes. Agreement with earlier investigations and with muonic x-ray measurements was maintained. One of the objects of the present paper is to report on new results with Ca^{40} at 250 and 500 MeV by which, in continuation of the progression we have reviewed, a new and more accurate charge distribution is deduced.

An extension of such measurements to other isotopes of calcium is desirable, and has greater promise of establishing quantitative contact with nuclear theory. Experimentally, a direct comparison of cross sections of various isotopes can produce more accurate results than separate, absolute measurements on the isotopes individually. The resulting isotopic differences in the charge distributions are consequently determined more accurately than those for individual nuclei. The first investigation of this kind was performed by Hahn, Hofstadter, and Ravenhall,[5] on the nuclei Fe^{56}, Ni^{58}, and Ni^{60}. The main part of the present paper presents an investigation along those lines of the isotopes Ca^{40}, Ca^{42}, Ca^{44}, Ca^{48}, and Ti^{48}. Preliminary results on some of these isotopes have been reported previously.[6,7] The most important product of the present investigation is the radial dependence of the isotopic differences in these charge distributions. To the information obtained from muonic and electronic x-ray isotope shift measurements, which is that the addition of neutrons changes the charge radius, we now add the detailed

* Work supported in part by the U. S. Office of Naval Research, Contract No. NONR 225(67), and the National Science Foundation.

† Present address: CERN, Geneva, Switzerland.

‡ Present address: Physikalisches Institut, Bonn, Germany.

§ Present address: Philips Research Laboratories, Eindhoven, Netherlands.

[1] B. Hahn, D. G. Ravenhall, and R. Hofstadter, Phys. Rev. **101**, 1131 (1956).

[2] H. Crannell, R. Helm, H. Kendall, J. Oeser, and M. R. Yearian, Phys. Rev. **121**, 283 (1961).

[3] M. Croissiaux, R. Hofstadter, A. E. Walker, M. R. Yearian, D. G. Ravenhall, B. C. Clark, and R. Herman, Phys. Rev. **137**, B865 (1965).

[4] D. G. Ravenhall, R. Herman, and B. C. Clark, Phys. Rev. **136**, B589 (1964).

[5] B. Hahn, R. Hofstadter, and D. G. Ravenhall, Phys. Rev. **105**, 1353 (1957).

[6] R. Hofstadter, G. K. Nöldeke, K. J. van Oostrum, L. R. Suelzle, M. R. Yearian, B. C. Clark, R. Herman, and D. G. Ravenhall, Phys. Rev. Letters **15**, 758 (1965).

[7] K. J. van Oostrum, R. Hofstadter, G. K. Nöldeke, M. R. Yearian, B. C. Clark, R. Herman, and D. G. Ravenhall, Phys. Rev. Letters **16**, 528 (1966).

information about how the charge distribution changes. A comparison is made with recent, muonic x-ray energy measurements.[8] These parallel in a very useful way the electron scattering investigation by providing the isotopic differences of the $K\alpha_1$ x-ray energy for the isotopes we have examined. There is very satisfactory agreement, to within experimental error, between the results of muonic x rays and electron scattering.

There are several reasons for making a concentrated study of the calcium isotopes. Experimentally, the nuclides can be obtained in nearly pure form isotopically, a desirable property for electron scattering targets. The range of atomic weight spanned is large, from $A=40$ to $A=48$, so that isotope effects are large and easier to measure. Two of the nuclei, Ca^{40} and Ca^{48}, have no low-lying excited states. The elastic and inelastic peaks are separated nicely, so that at large recoil momenta, where elastic peaks are small, they can be measured even in the presence of large inelastic contributions. Differential cross sections can be measured at large angles and/or high energies. Thus the ends of the isotopic chain are anchored on very reliable nuclei.

These same reasons make the nuclei interesting from a theoretical viewpoint. It may be hoped that, generally, nuclear theory can make predictions about isotopic differences more easily than it can describe the whole charge distribution. From the viewpoint of the shell model, both Ca^{40} and Ca^{48} are doubly magic nuclei, and the charge distributions of the intervening isotopes reveal the effect on the proton closed shells of the addition of neutrons in the $1f_{7/2}$ shell.[9] The behavior of protons in this shell is obtained by looking at Ti^{48}. Comparisons of some of our results with the shell model have been made already by Gibson and van Oostrum[10] and by Swift and Elton.[11] It is possible that our results on the charge distributions show where the crude independent particle-shell model is inadequate. An investigation along that line will be presented in a forthcoming paper.[12] The charge distributions presented in the present paper, obtained with a phenomenological charge shape with adequate flexibility, make no reference to a particular nuclear model. They are thus suitable for comparison with other nuclear models, and hopefully will serve as useful checks on radial dependences.

In the body of the paper we comment more fully on the question of nuclear polarization, i.e., on whether virtual nuclear excitation spoils the simple dependence of the charge distribution on the ground-state nuclear wave function. The polarizability of a nucleus may depend on the closeness of the low-lying excited states. Also, it probably affects differently electron scattering and muonic x rays. The close agreement of these two methods reported in this paper, with neglect of nuclear polarization in each case, is perhaps an indication that nuclear polarization is not important at the present level of accuracy. The present work lays the foundation for a detailed examination of the energy dependence of the electron scattering process,[13] another place where nuclear polarization may be revealed.

II. EXPERIMENTAL PROCEDURE

Since the experimental arrangements used in electron scattering experiments at Stanford have been described previously by various authors,[14] we give only a brief survey of the equipment and emphasize those features that have been essential for our experiment.

Electrons from the Stanford Mark III linear accelerator with energies up to 500 MeV were analyzed by a system of two analyzing magnets and a pair of slits. The electron energy had been calibrated against the current in the first deflection magnet,[15] and the desired value was set after saturating the magnet for a period of 1 min. The beam was focused on the target placed in the center of the scattering chamber, around which the 72-in. spectrometer was rotated.[14] The position of the beam spot on the target could be adjusted by a set of Helmholtz coils downstream from the analyzing magnet system; the spot dimensions were minimized by setting the currents through various quadrupoles in the system. Targets of the various isotopes were mounted in a target ladder described by Crannell.[16]

After the electron beam had traversed the scattering chamber, it was absorbed in a Faraday cup,[14] where the electron beam was collected and integrated. Because of the different thickness of materials used, the efficiency for collecting the beam was not the same for all targets. A secondary emission monitor, placed behind the target with a larger beam acceptance solid angle than the

[8] R. D. Ehrlich, D. Fryberger, D. A. Jensen, C. Nissim-Sabat, R. J. Powers, V. L. Telegdi, and C. K. Hargrove, Phys. Rev. Letters **18**, 959 (1967). We thank Dr. Ehrlich for the more recent value of the Ca^{40} energy quoted in Table IV, and both him and Professor Telegdi for discussions.

[9] The theoretical interest in Ca^{40} and Ca^{44} was pointed out to R. Hofstadter by Professor A. de-Shalit.

[10] B. F. Gibson and K. J. van Oostrum, Nucl. Phys. **A90**, 159 (1967).

[11] A. Swift and L. R. B. Elton, Phys. Rev. Letters **17**, 484 (1966). Reference to other contributions by this group is contained in L. R. B. Elton, Phys. Rev. **158**, 970 (1967).

[12] L. R. Mather, J. M. McKinley, and D. G. Ravenhall (to be published).

[13] Preliminary results of electron scattering from Ca^{40} and Ca^{48} at 750 MeV have been reported by some of us: J. B. Bellicard, P. Bounin, R. F. Frosch, R. Hofstadter, J. S. McCarthy, F. J. Uhrhane, M. R. Yearian, B. C. Clark, R. Herman, and D. G. Ravenhall, Phys. Rev. Letters **19**, 527 (1967). The modifications in resulting charge distribution that these experiments suggest are an order of magnitude smaller than the isotopic differences reported in the present paper, and so do not affect them appreciably. This is discussed in Sec. X.

[14] For details on some part of the experimental apparatus the reader is referred to the various papers compiled by R. Hofstadter, in *Nuclear and Nucleon Structure* (W. A. Benjamin, Inc., New York, 1963). See especially pp. 237–239 and pp. 639–641.

[15] T. Janssens, Ph.D. thesis, Stanford University, 1965 (unpublished).

[16] H. Crannell, Phys. Rev. **148**, 1107 (1966).

TABLE I. Target data.

Isotope	Isotopic abundance (%)	Target thickness (mg/cm²)
Ca^{40}	99.97	529
Ca^{42}	94.4	501
Ca^{44}	98.4	513
Ca^{48}	97.2	487
Ti^{48}	...	460

Faraday cup, was used to measure this efficiency in each case. Even with the Faraday cup at the closest possible distance to the target (at scattering angles larger than 40°) there was a slight difference in efficiency from target to target and small corrections were necessary.

The enriched calcium and titanium targets used in this experiment were prepared for our use by the Oak Ridge National Laboratory. The enrichment factors measured by Oak Ridge and thicknesses are given in Table I. The approximate surface dimensions of all calcium targets were 1.0×0.75 in.; the Ti^{48} target was slightly smaller (1.0×0.6 in.). This similarity in size and thickness among the targets was necessary because it excluded possible errors due to using different geometry for each target with respect to spectrometer, Faraday cup, and electron beam.

The main contamination in the Ca^{42}, Ca^{44}, and Ca^{48} targets was the most abundant isotope Ca^{40}. In the comparative measurements, the cross-section ratio found in the experiment was corrected for this impurity. Apart from this isotopic impurity, it is known that the Ca^{48} target was contaminated by a slight oxygen impurity. We have observed a small peak which shifts in energy exactly as an oxygen elastic peak would. Corrections have been made for this contamination. The spectrum of Ca^{40} did not show any contamination.

The 72-in. spectrometer has been equipped with a 100-channel ladder detector,[17] with which spectra of scattered electrons could be measured in an energy interval covering 8% of the incident energy, sufficient to contain all peaks due to level structure in the target nucleus at the energies used in this experiment. The output of this 100-channel ladder was stored on magnetic tape and processed with the IBM 7090 computer of the Stanford Computation Center. The relative efficiencies of the channels for counting electrons were measured in a way described by Crannell and Suelzle[18] and were used for correcting the data in a computer program for plotting the spectra. Several spectra drawn from the output of this program are shown in Figs. 1–5.

Each figure shows two spectra, each consisting of 100 points corresponding to the 100 channels in the ladder detector. The points indicated by open circles make up the measured spectrum corrected for relative efficiencies; the vertical axis gives the number of scattered electrons per unit momentum interval and integrated charge, the horizontal axis gives the value of the scattered momentum. Measured values for the dispersion parameters of the 72-in. spectrometer were used

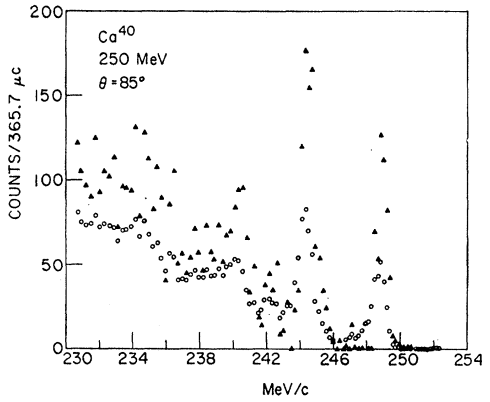

FIG. 1. The spectrum of scattered electrons from Ca^{40}, with an incident energy $E_0=250$ MeV, at an angle $\theta=51°$. The open circles are the measured points, which after correction for radiation losses, as described in Sec. II, become the solid triangles.

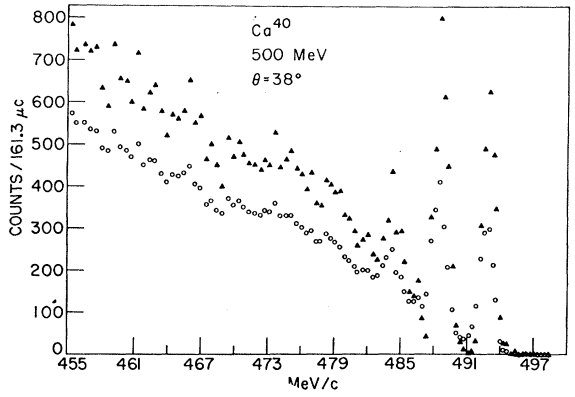

FIG. 2. As in Fig. 1, with $E_0=500$ MeV and $\theta=38°$.

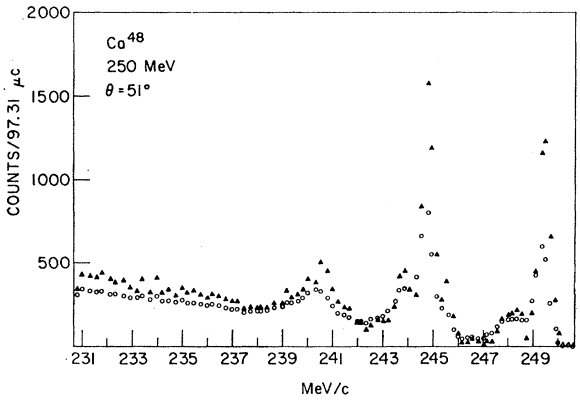

FIG. 3. The spectrum of scattered electrons from Ca^{48}, with $E=250$ MeV, $\theta=51°$, as described in the caption to Fig. 1.

[17] L. R. Suelzle, Ph.D. thesis, Stanford University, 1967 (unpublished).

[18] H. L. Crannell and L. R. Suelzle, Nucl. Instr. Methods 44, 133 (1966).

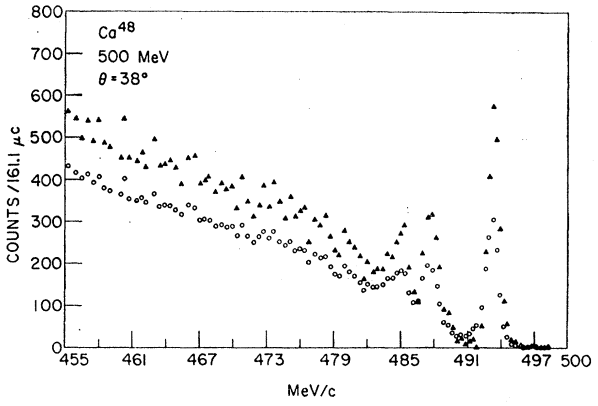

FIG. 4. As in Fig. 3, with $E_0=500$ MeV, $\theta=38°$.

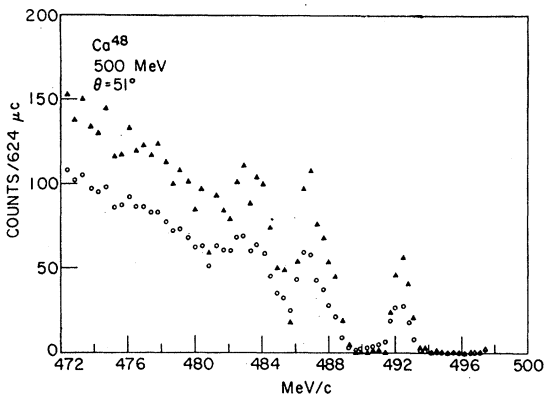

FIG. 5. As in Fig. 3, with $E_0=500$ MeV, $\theta=51°$.

in the momentum calibration of the horizontal axis and also for the determination of the momentum interval spanned by one channel, which is used in the calibration of the vertical axis. Note that the absolute momentum values on the horizontal axis might not be accurate, owing to absolute calibration errors, but the energy differences are presumed to be correct.

The 100 points indicated by black triangles in the same figures illustrate the result of the "unfolding" procedure executed in the same computer program. These points show the fictitious spectrum as it would have been measured in the absence of three effects giving rise to tails at the low-energy side of a peak. These three effects are: bremsstrahlung of the electrons in the target material, emission of Schwinger radiation at the collision with the target nucleus, and energy loss by Landau straggling. Starting from the channel with the highest scattered momentum, the unfolding program calculates how many electrons originally had an energy within a channel and to what channels they have been degraded by losing energy from each of the three effects mentioned. The measured number of electrons in that channel as well as that in all channels with lower energy are corrected by the calculated function. This procedure is repeated subsequently for lower channels. A similar procedure for correcting spectra measured with a 100-channel ladder for the first two radiative effects only has been described by Crannell.[16] Although we use the same basic formulas for the radiative losses, our procedure uses the channels as momentum intervals with a width varying over the ladder instead of the energy "bins" with constant width used in the method described in Ref. 16.

The effect of the unfolding procedure on the spectrum is illustrated in Figs. 1–5. In each case the peaks in the unfolded spectrum are narrower than in the original spectrum and the tails of the peaks have disappeared, reducing the ordinate to values close to zero in regions where no inelastic peaks are present (e.g., Ca^{40} in Fig. 1). Tests on this unfolding procedure have been performed by calculating a Ca^{40} elastic cross section from the unfolded spectrum as well as from the original one by cutting off at 2.5 MeV below the elastic peak and correcting for the rest of the tail by a hand calculation. The results agreed well to within the error in the determination of a peak area. Application of this unfolding program separated the elastic peak from the first inelastic peak completely in almost every case. Adding the counts under the unfolded elastic peak and multiplying this amount by a factor containing integrated charge, solid angle, target thickness, and other parameters gave the scattering cross section directly in microbarns per steradian.

The absolute cross-section determination of Ca^{40} and the measurement of the cross-section ratio between two neighboring nuclei are essentially both comparison measurements. In the first case the electron scattering yield from a Ca^{40} target is compared with that from the hydrogen nuclei in a polyethylene target, whereas the scattering yields from different calcium or titanium targets are compared directly in the second case. For the absolute calibrations the target ladder contained a rotating polyethylene disk and a carbon target for correcting the scattering yield from polyethylene (CH_2) for the background from carbon nuclei.[16] Moreover, several other targets of various isotopes and a luminescent crystal for observing the beam position could be mounted simultaneously in the target assembly. Moving the ladder up and down in well-defined steps brought each target quickly into exactly the same position with respect to spectrometer and electron beam. This feature was important because it is desirable that the geometry of the experiment should remain unchanged during a comparison, as discussed in Sec. IV. Our procedure thus consisted of taking alternative spectra of various calcium or titanium targets, checking the beam position with the crystal in the same target position, and taking absolute calibration points with the polyethylene disk. Moreover, we observed the following rules:

1. The elastic peaks in the two spectra were counted in the same part of the ladder detector in order to reduce the influence of possible errors in the dispersion

parameters which are used in the determination of the relative efficiencies of the channels. It was most convenient to use channels 80 through 90 for the elastic peak, because the dispersion of the spectrometer is largest in this region.

2. The time of measurement for each target was limited to 30 min in order to reduce influence of long-term drift of beam energy and position. In order to reach the required number of counts for good statistics, the same comparison was repeated several times.

3. The counting rate was limited to one count per 10 beam pulses per channel, so that the counting rate correction applied in the plotting program was kept low in each case. Visual observation of the data accumulating together with a "clock" channel on the display of the 100-channel ladder made the fulfillment of this requirement quite easy.

III. EXPERIMENTAL RESULTS

The elastic scattering yields from the five available targets (see Table I) were compared, two at a time, according to the following scheme:

Ca^{40}-Ca^{42}, Ca^{40}-Ca^{44}, Ca^{40}-Ca^{48}, and Ca^{48}-Ti^{48}.

The cross sections of the "basic nucleus" Ca^{40} were calibrated absolutely with hydrogen during each of these comparison runs, so that we collected a large amount of data on this absolute determination. We took Ca^{48} rather than Ca^{40} as a comparison target for Ti^{48} because of the similarity in target thickness and mass number between these two targets.

Most of our results were obtained at a fixed energy, either 250 or 500 MeV, in order to facilitate fitting of the data with phase-shift–analysis calculations. Only the absolute cross sections of Ca^{40} and the Ca^{40}-Ca^{48} comparison could be measured at the higher energy, because the lowest levels of these nuclei occurred at sufficiently high excitation energy to be separated from the elastic peak. (The oxygen contamination in the Ca^{48} target mentioned in Sec. II corresponded to a much higher recoil and could cause no trouble at the measured angles at 500 MeV.)

Besides the main data at 250 and 500 MeV, some ratio measurements were made at lower energies. The geometry of our experimental arrangement prevented the spectrometer from being set at deflection angles smaller than 32°, and in order to obtain results at low values of the momentum transfer q, points were taken at the smallest possible angle $\theta=32°$, and at lower energies. As is justified in Sec. XII, one may transform the cross-section ratio at this lower energy to an angle lower than 32° at 250 MeV and the same value of momentum transfer q, according to the expression $q=2E_0\sin\frac{1}{2}\theta$. In this way we obtained information for the comparisons at low values of q, where both nuclei tend to look like points to the incoming electrons and therefore do not show much structure difference. This gives a good check on our method of measurement, especially on the ratio of target thicknesses used in the calculation of cross-section ratios.

Table II shows all of our results for the absolute cross section of Ca^{40} and for the values of cross-section ratios, given in the form

$$D=\frac{(d\sigma/d\Omega)_A-(d\sigma/d\Omega)_B}{(d\sigma/d\Omega)_A+(d\sigma/d\Omega)_B}, \tag{1}$$

when the two nuclei A and B are compared. The angular acceptance $\Delta\theta$ of the spectrometer was 1.8° at most angles, but was reduced at the smaller angles to the values indicated in the footnotes to the table. Separate entries are given at some angles for results obtained with different values of $\Delta\theta$.

IV. ACCURACY OF EXPERIMENTS

As mentioned in Sec. II, the Ca^{40} absolute cross sections were determined from a comparison with the measured hydrogen cross section, and the D values were obtained from a comparison between targets of two neighboring nuclei. The reason that we could measure some D values with errors of only 1%, and absolute Ca^{40} cross sections with only an 8% relative error, lies in the choice of the comparison target used in the two kinds of experiment.

One can see the reason for this difference in accuracy by summing up the various sources that contribute to the experimental error in both cases:

1. The energy of the incoming electrons is calibrated by measuring the current through the analyzing deflection magnet, as described in Sec. II. The reproducibility error in the energy set by this method was found to be 0.5% in this experiment. The energy dependence of the Ca^{40} cross section is quite different from that of the hydrogen cross section, so that the absolute Ca^{40} measurements are greatly influenced by this kind of error. The D measurements, on the other hand, are much less influenced by an energy error, since in this case two nuclei are compared with about the same cross-section values for most angles, so that the D-value ratio is much less dependent on the energy setting, as long as the energy does not change during a comparison. It is felt that this reproducibility error in the energy is one of the main sources of error in the absolute Ca^{40} measurements. Because data were collected over a large number of runs and thus the energy was frequently set to the quoted energy, this error contributes to the inaccuracy of each individual point, in contrast to the inaccuracy of the floating wire calibration of the deflection magnet, which affects the whole cross-section curve as a systematic error in the quoted energy. This last error is estimated to be of the same order of magnitude.

TABLE II. Experimental results. The differential cross sections are in the laboratory frame, in microbarns per steradian, with the appropriate power of 10 indicated in parenthesis. The quantity D is the difference divided by the sum of differential cross sections for the two isotopes quoted, the difference being taken in the order indicated. Tables II(a) and II(b) refer to an incident energy of 250 MeV, except for the first entries, where the incident energy, in MeV, is indicated in parentheses following the angle, and Table II(c) refers to 500 MeV. The angular acceptance $\Delta\theta$ is 1.8° (i.e., ±0.9°) except for the smaller angles, where the value of $\Delta\theta$ is as indicated in the footnotes.

a. Experimental results at 250 MeV.

θ deg	$d\sigma/d\Omega$, Ca^{40} μb/sr	$D(Ca^{40}$-$Ca^{48})$ %
32(175)	...	−0.1±1.4[a]
32(200)	...	0.6±1.5[a]
32	(6.34±0.45)(2)[b]	1.1±1.0[c] 1.3±1.0[a]
35	(2.77±0.20)(2)[b]	0.5±1.0[c] 4.9±1.5[a]
37.5	(1.40±0.10)(2)[b]	0.7±1.0[c] 2.9±1.4
40	(5.89±0.35)(1)	3.2±1.0 6.0±1.5
42	(3.25±0.30)(1)	4.9±1.0
44	(1.61±0.10)(1)	9.6±1.0
46	(7.95±0.80)(0)	9.2±1.0 11.7±1.4
47	(5.32±0.50)(0)	10.2±1.3
48	(3.46±0.25)(0)	11.6±1.0
49	(2.40±0.25)(0)	12.8±1.3
50	(1.62±0.15)(0)	11.3±1.2 11.5±1.0
51	(1.19±0.10)(0)	7.5±1.0
52	(8.27±0.40)(−1)	− 0.3±1.0
53	...	− 4.6±1.0
54	(5.38±0.40)(−1)	−12.9±1.9 −13.2±1.6
55	(4.71±0.50)(−1)	−17.6±2.1
56	(4.32±0.30)(−1)	−19.7±1.7
58	(4.50±0.45)(−1)	−24.0±1.7 −21.3±2.2
60	(4.82±0.30)(−1)	−22.6±1.7
62	...	−19.7±1.5
64	(4.54±0.30)(−1)	−18.9±1.5
68	(3.24±0.25)(−1)	−16.2±1.5
72	(2.11±0.15)(−1)	−13.0±1.3
76	(1.18±0.10)(−1)	−12.1±1.5
80	(6.12±0.40)(−2)	− 7.2±1.5
85	(2.23±0.15)(−2)	− 4.8±1.4
90	(6.50±0.45)(−3)	1.7±2.0
95	(1.42±0.10)(−3)	17.9±3.0
100	(2.70±0.35)(−4)	−20.4±12
105	(2.13±0.25)(−4)	−52.7±11
110	(3.92±0.45)(−4)	−25.0±8.0
115	(3.13±0.55)(−4)	−48.9±13
125	(2.21±0.30)(−4)	−30.4±11

b. Experimental results at 250 MeV.

θ deg	$D(Ca^{40}$-$Ca^{42})$	$D(Ca^{40}$-$Ca^{44})$ D in %	$D(Ca^{48}$-$Ti^{48})$
32(150)	...	...	−7.9±1.2[a]
32(175)	...	...	−5.7±1.6[a]
32(200)	...	...	−5.2±1.8[a]

b. Experimental results at 250 MeV.

θ deg	$D(Ca^{40}$-$Ca^{42})$	$D(Ca^{40}$-$Ca^{44})$ D in %	$D(Ca^{48}$-$Ti^{48})$
36(175)	1.4±0.7[a]	...	...
32	2.7±0.9[a]	1.3±1.0[d]	0.4±1.0[c] 1.3±1.2[a]
35	...	3.0±1.0[d]	2.7±1.1[c] −0.2±1.5[a]
36	3.3±0.8[a]	...	...
37.5	...	6.4±1.0[d]	4.1±1.0[c] 3.4±1.4
40	5.3±1.0[a]	5.7±0.8	4.3±0.7
42	...	6.1±1.0	5.0±1.0
44	5.4±1.0[a]	8.0±0.8	5.4±0.8
46	...	8.7±1.0	6.1±1.0
48	8.2±1.0	12.3±0.9	3.4±1.0
50	8.5±1.5	9.1±0.9	− 7.2±0.7
52	5.2±1.0	5.8±0.7	−16.1±1.5
54	0.4±1.4	−4.8±1.0	−19.3±1.5
56	−2.9±1.5	−8.7±1.1	−19.9±1.5
58	...	...	−16.1±1.4
60	−1.0±1.0	−9.0±1.1	−10.5±1.2
62	...	...	− 7.4±1.2
64	−0.4±1.3	−5.7±1.0	− 4.8±1.2
66	...	...	− 1.1±1.5
68	−0.1±1.3	−4.4±1.5	1.8±1.4
70	...	...	4.0±1.4
72	2.3±1.5	−0.5±1.0	5.5±1.4
74	...	...	11.4±2.0
76	3.9±1.5	0.3±1.5	8.6±1.4
80	6.5±1.4	4.0±2.0	17.5±1.4
84	10.3±2.4	...	...
85	...	5.6±2.4	20.9±2.4
90	...	12.5±3.1	34.9±3.0

c. Experimental results at 500 MeV.

θ deg	$d\sigma/d\Omega(Ca^{40})$ μb/sr	$D(Ca^{40}$-$Ca^{48})$ %
32	(1.68±0.12)(0)[a]	−17.1±0.9[a]
35	(8.40±0.60)(−1)[a]	−13.6±1.0[a]
38	(2.98±0.22)(−1)[a]	− 7.6±1.0[a]
40	(1.26±0.09)(−1)[a]	− 1.7±1.1[a]
42	(4.35±0.44)(−2)[a]	6.8±1.7[a]
44	(9.83±0.64)(−3)[a]	17.1±2.6[a]
46	(2.34±0.28)(−3)[a] (2.66±0.23)(−3)	−14.9±5.1[a] −19.5±3.1
48	(2.21±0.16)(−3)	−47.1±2.1
51	(3.50±0.22)(−3)	−36.1±1.5
54	(2.98±0.26)(−3)	−27.9±2.4
57	(1.85±0.22)(−3)	−18.4±4.2
60	(7.98±0.80)(−4)	−11.7±5.2
63	(2.58±0.41)(−4)	...

[a] $\Delta\theta=0.9°$.
[b] $\Delta\theta=0.3°$.
[c] $\Delta\theta=0.36°$.
[d] $\Delta\theta=0.2°$.

2. The deflection angle θ is set with an uncertainty of less than 0.1°. This error also contributes to the error bar of each absolute cross section, but is again negligible in the measurement of D for the same reason as given in item 1.

3. In general, absolute calibration errors in the integration of the beam current are removed by comparing scattering yields in both kinds of measurements. However, if the comparison target is CH_2 instead of a material with about the same cross section, the counting rates of the electrons scattered from each target are sometimes completely different, so that one has to apply different beam currents and different integrator settings. In such a case the sensitivity of the current

integrating device might vary for the two targets, which contributes to the error bars of the absolute points.

4. In order to get an accurate ratio measurement, the geometry of the two targets should be similar. This is necessary, not only because the solid angle of the targets with respect to the spectrometer should remain unchanged, but also because a small part of the beam might miss the target and this percentage, although small in itself, might be different for targets of unequal thickness. This effect might be important at larger angles. Obviously this requirement is more easily fulfilled in the D measurements using Ca targets of equal density, surface, and about the same thickness, than in the absolute Ca^{40} measurements.

5. Another source of error, due to a geometrical effect, arises from a possible variation of beam position on the target during a comparison. The 2-in.-thick entrance slits of the spectrometer have a collimating effect, if the slit width is comparable to the size of the beam spot (0.25 in.). This is the case at lower angles, where the cross section is high and the spectrometer slit width must be reduced to 0.5 in or less. Since a low beam current is used to reduce the high counting rate of scattered electrons, it is very difficult to notice any shift in beam position during a comparison at these low angles. The resulting change in angular position and solid angle, and thus of measured cross-section ratio, is believed to be the main contribution to the error in the D measurements at low angles.

6. Counting statistics in cross-section measurements become an important source of error at the largest angles where the cross section is low. At lower angles, however, this error is always smaller than the inaccuracies mentioned above. Moreover, the relative efficiencies of the 100 channels are also measured with an error of 1%, due to counting statistics.

7. Besides the source of error mentioned in the six items discussed above, there are some additional disadvantages inherent in the use of CH_2 as a comparison target. The subtraction of the carbon background mentioned in Sec. II contributes to the error with which the calibration H cross section is measured. The H peak itself is much broader than an elastic Ca peak (the energy spread due to proton recoil is observed in the angular acceptance of the spectrometer), so that a larger and different part of the 100-channel ladder has to be used. Therefore, the accuracy with which the dispersion parameters and the channel width are known affects the accuracy of the comparison with hydrogen. If the two compared targets have different atomic numbers, such as H and Ca, the radiative corrections in the unfolding program become quite different. Any inaccuracy in the theory, according to which these corrections are calculated, will result in a systematic error in the absolute Ca^{40} cross sections.

In short, one may say that all seven items mentioned above contribute to the errors in the absolute Ca^{40} measurements, whereas only items 5 and 6 are the main sources of error in the D determinations. All these contributions have been taken into account in assigning the error bars quoted in Table II, where some measurements have been averaged over a number of trials at the same energy and angle. The errors in the D values of Ca^{40}-Ca^{48} at the largest angles have been somewhat enlarged, because the large angle of the target with respect to the beam (up to 60°) made it very hard to prevent the beam spot from partially missing the targets. Note, however, that much better information about this part of the curve has been obtained at 500 MeV, at smaller angles and higher cross sections. Finally, a systematic error of $\pm 1\%$ is estimated for all the D measurements to take into account inhomogeneities in the targets and an error in target thickness ratio.

V. THEORY

As has been customary in electron-nucleus scattering, the basic assumption will be made that the nucleus can be represented by a static charge distribution. We are well aware of the certain presence, and the possibly appreciable effect, of nuclear polarization, i.e., virtual excitation, in the scattering process. A recent study of this phenomenon has been made by Rawitscher.[19] He explores some of the possible effects that nuclear polarization can have on the elastic scattering process, in terms of a simplified model. We describe his calculation in some detail, to explain why we have not used it in our analysis. The scattering process is described by two coupled channels, one being the usual elastic scattering channel, in which the nucleus is in its ground state, the other channel representing all inelastic scattering. A coupling between these channels thus produces on the elastic scattering the effects of both virtual nuclear excitation, and the depletion of flux due to the real inelastic scattering. For a number of reasons the actual calculation must fall short of describing the real process. While the average strength of the coupling between the channels can be chosen to give the observed total inelastic scattering, its radial shape is not known, and must be assumed. For computational simplicity, the coupling is taken to have the multipole character of an electric monopole. The excitation energy of the inelastic channel is ignored, so that possible dependence of the effect on the proximity to the ground state of excited levels, a feature by which Ca^{42} and Ca^{44} differ markedly from Ca^{40} and Ca^{48}, is not examined. In the final result, the rather small changes produced on the elastic cross section appear to be of just the kind that small modifications in the static charge distribution would produce in single-channel scattering.

A calculation somewhat more elaborate in scope, and consequently more difficult to perform, has been re-

[19] G. H. Rawitscher, Phys. Rev. **151**, 846 (1966). References to earlier work on nuclear polarization are cited in this paper.

ported by Onley.[20] He includes electric dipole and quadrupole excitations, but ignores the nuclear excitation energy. A comparison with Rawitscher's result on calcium shows that the order of magnitude of the effect is the same, i.e., not very dependent on multipolarity. The addition to the cross section is smoothly varying with angle, and thus appears relatively most important at the diffraction minima (about a 14% effect at the 100° minimum in Ca^{40} at 250 MeV). Furthermore, a comparison of Onley's results at two different energies, 250 and 600 MeV, for Ni^{58}, suggests that the effect is dependent largely on q, the recoil momentum, and not separately on energy and angle. (This may be a consequence of ignoring the nuclear excitation energy.) The effect on the elastic cross section of a small change in a charge distribution parameter, for example, c, is qualitatively of just the same character. A report of the results of nuclear-polarization calculations in the form of the effective change produced in the monopole charge distribution would help considerably in estimating how important the effect appears to be. As regards utilization of Onley's method, we note that his approach, simplified as it is by ignoring nuclear excitation, produces cross sections to an accuracy of 1%. To analyze our isotopic differences effectively, it will be necessary to improve on this.

Another relevant calculation of nuclear polarization has been reported by Toepffer.[21] He uses the eigenchannel method of Danos and Greiner,[22] and does not ignore the nuclear excitation energy, although he uses for the monopole density a uniform charge distribution. As regards order of magnitude, his results are compatible with those of Onley[20] and Rawitscher.[19] His conclusions about the effectiveness of high-lying (1−) nuclear states may indicate, however, that it is important not to neglect nuclear excitation energy.

In all these calculations the transition form factor or its equivalent is assumed, the object being to deduce from elastic scattering something about this assumption. It is important to appreciate that the measured quantity is the elastic scattering, not the static charge distribution. The charge distribution has been obtained on the assumption that it describes the complete scattering process. Apart from energy dependence, it may be impossible to distinguish an added polarization contribution from the effect of equivalent changes in that static charge distribution itself. We therefore surmise that it is impossible to detect in the elastic scattering, at one energy or even over a range of energies, the nuclear polarization. What is needed is an accurate prediction of the effect, from nuclear theory and inelastic electron scattering experiment, so that it may be included as a necessary, known complication of the elastic scattering process. More work is needed before such a program can be carried out. Our analysis must therefore ignore nuclear polarization, and assume, for want of a better practicable model, that the nucleus affects the electron only as a real, static charge distribution.

[20] D. S. Onley, Nucl. Phys. (to be published).
[21] C. Toeppfer, Phys. Letters **26B**, 426 (1968).
[22] M. Danos and W. Greiner, Phys. Rev. **146**, 708 (1966).

VI. CALCULATIONS

The methods by which the Coulomb potential of the charge distribution is inserted into the Dirac equation, and a partial-wave analysis performed to obtain the differential cross section, are essentially the same as those described previously.[23] All calculations are performed in double-precision arithmetic on an IBM 7094 computer at the Research Laboratories, General Motors Corp. The cross sections are calculated to much greater accuracy than it is possible to measure them, of course. The method employed to analyze the isotopic differences in cross sections involves examining small differences of theoretical cross sections. Because of the high accuracy it can be carried out unhindered by small numerical inaccuracies. The incident energy used in the calculations is reduced from the actual incident energy by 0.5 MeV, the average energy loss of the electrons in the target. The effect of nuclear recoil is taken into account to order v/c by carrying out the partial-wave analysis in the electron-nucleus center-of-momentum frame, and then transforming the differential cross section to the laboratory frame.[24] The angular resolution of the spectrometer is folded into this cross section, and the result compared with experiment by means of a least-squares analysis. The effect on the differential cross section of this angular folding is important, especially at small angles. On the cross-section differences D, Eq. (1), however, it is quite small, $\sim 0.02\%$ at $\theta \sim 30°$ for the Ca^{40}-Ca^{48} results at 250 MeV, for example.

VII. CHARGE DISTRIBUTIONS

For the most part, the shape used to parameterize the nuclear charge distributions is that called previously the parabolic Fermi:

$$\rho(r)=\rho_0[1+wr^2/c^2]\{\exp[(r-c)/z]+1\}^{-1}. \quad (2)$$

It has three adjustable parameters c, z, and w. The values taken by these parameters for the nuclei examined here, and their relationship to the familiarly defined half-radius $r_{0.5}$ and 90–10% surface thickness t, are discussed in Secs. IX and XIV. There is some evidence that the choice (2) is a logical improvement over previous shapes. In analyses of Ca^{40} scattering at 183 MeV[3] and 250,[4] it was found that among a variety of smoothed uniform shapes the Fermi shape [$w=0$ in Eq. (2)] gave best agreement. This already

[23] The basic methods we use are described in D. R. Yennie, D. G. Ravenhall, and R. N. Wilson, Phys. Rev. **95**, 500 (1954); and in Ref. 3.
[24] L. L. Foldy, K. W. Ford, and D. R. Yennie, Phys. Rev. **113**, 1147 (1959).

means that more information than just the two parameters c and t has been obtained. To improve the fit to the present data at large angles, especially for the Ca^{40}-Ca^{48} difference, additional flexibility is needed. The inclusion of the parameter w, to be varied together with c and z, is one way of achieving this flexibility. After introducing our main results, we return in Sec. X to a discussion of the suitability of this choice.

VIII. ANALYSIS OF ISOTOPIC DIFFERENCES

In the original exposition of the isotopic difference measurements,[5] a simple method was described in which the dependence of the cross-section difference D, Eq. (1) of Sec. III, on the parameters of the charge distribution is approximated by the first term in a series expansion in each parameter. The individual cross sections, as exemplified by Fig. 6, show a diffraction structure which depends in a rather simple way on the charge distribution. In a manner relatively independent of the nuclear shape chosen, the cross-section difference

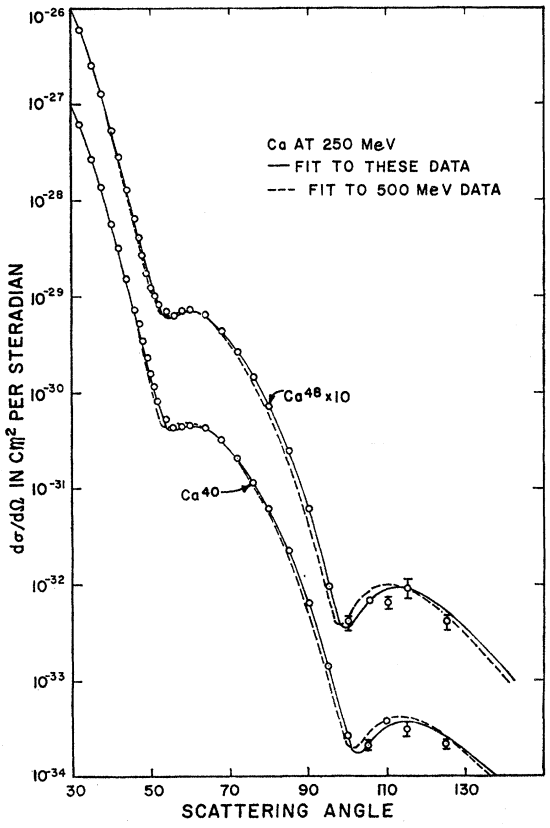

FIG. 6. Differential cross sections for scattering of 250-MeV electrons by Ca^{40} and Ca^{48}. Because of an average energy loss in the target of 0.5 MeV (see Sec. II), the incident energy used in the calculation is 249.5 MeV. The experimental points are those given in Table IIa, and the full curves are the best fits to these data with the phenomenological shape (2) of Sec. VII containing the parameter values given in the first and fourth rows of Table III. The dashed curves are for the best fits to the 500-MeV data, as described in Sec. XII.

resulting from a change in the value of each parameter has a certain characteristic dependence on angle. For Ca^{40}, the curves in Fig. 7 show the expected behavior of the function D, Eq. (1), when a neighboring isotope has one of its parameters c, z, or w, changed by a small amount, assuming that the dependence is linear. These come from partial-wave calculations, of course, as do all of the results we report. It is possible to explain them simply, nonetheless. The character of the Δc curve is understood by recalling that an increase in c shifts the whole diffraction pattern to q values ($q=2E_0\sin\frac{1}{2}\theta$) smaller by $\Delta c/c$. The resulting quantity D is then the oscillating function shown with two distinct "edges." The positions of the edges are determined by the c of Ca^{40}, and the peak-to-valley value is proportional to Δc. An increase in z alone, i.e., a smoother surface, causes the cross section to decrease more rapidly with angle, so that the resulting D is a smoothly increasing function. The effect on cross sections of the third parameter w is, very qualitatively, to shift the position of the second diffraction maximum with respect to the first. In the resulting D, it reproduces to some extent the curve with Δc, but with a different relative size for the two edges.

The linearity assumption allows us also to combine these curves additively, in appropriate proportions, to represent the result of simultaneous changes in all of the parameters. By comparison with the experimental results, one can obtain by inspection rough estimates of the actual differences in parameter values, Δc, Δz, and Δw between the two isotopes. With only two parameters Δc and Δz, the peak-to-valley value of the first edge determines Δc, while the position of its center determines Δz. The function of the third parameter Δw is to allow the relative sizes of the two edges to be changed. Thus Δw is determined most accurately for the Ca^{40}-Ca^{48} difference, where the experimental data cover the second edge completely. The similarity between the Δc and the Δw curves makes evident their strong linkage; Δw is not a completely independent new parameter. It is important to remember this when considering errors on those parameters and their effect on the charge distribution. The method also displays the sensitivity of the parameter changes to some experimental errors. For example, an over-all shift of the fit vertically is achieved by modifying the surface thickness change Δz (or Δt). An experimental uncertainty in target thickness, which means an over-all uncertainty in the vertical scale (for our targets, estimated to be about $\pm 1\%$) therefore affects mainly the prediction of the Δz value. (The values of Δc and Δw are affected also, but in a compensating way.) This is in fact the main source of the error in the parameters, so far as the isotopic differences are concerned.

The parameter differences obtained in the present work are large enough, however, that the method must be modified. An expansion is made not about zero changes in the parameters of the two isotopes, but

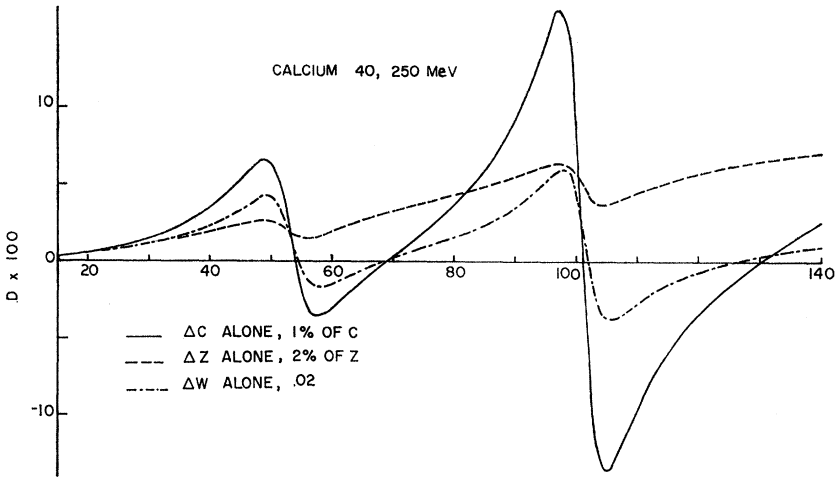

FIG. 7. Calculated $D(\theta)=[\sigma_{40}(\theta)-\sigma'(\theta)]/[\sigma_{40}(\theta)+\sigma'(\theta)]$ versus scattering angle θ, for 250-MeV electrons on Ca. The differential cross section $\sigma_{40}(\theta)$ comes from the charge distribution (2) with the Ca^{40} parameters c, z, and w given in the first row of Table III. The three curves shown come from cross sections $\sigma'(\theta)$ in which one of c, z, and w is increased by 1%, 2%, and 0.02, respectively. The behavior and utility of these curves is discussed in Sec. VIII.

about their approximate actual values. The expansion also depends a little on the parameter values themselves, and so must be carried out separately for each assumed shape in either Ca^{40} or Ca^{48}. The method is too tedious to be given in detail but can be reconstructed from the above description.

IX. FITTING TO 250-MeV EXPERIMENTS

The experimental information at 250 MeV comprises individual differential cross sections with experimental errors of order $\pm 8\%$, and isotopic differences D between pairs of isotopes measured to about $\pm 1\%$ at the smaller angles. The isotopes Ca^{40} and Ca^{48} provide the most accurate and extensive information. To utilize the increased accuracy of the difference measurements, we make a least-squares fit to the separate Ca^{40} and Ca^{48} differential cross sections, and also to the measured isotopic differences. Specifically, for each point on a mesh of c, z, w values of Ca^{48}, we fit to the Ca^{48} cross section, obtaining $\chi^2(48)$. The fit to the isotopic difference determines the changes in c, z, and w, for a minimum $\chi^2(40-48)$. The predicted c, z, w for Ca^{40} are then used to obtain the $\chi^2(40)$ for the Ca^{40} cross section. The first sets of parameter values for Ca^{40} and Ca^{48} quoted in Table III minimize the sum

$$\tfrac{1}{2}[\chi^2(40)+\chi^2(48)]+\chi^2(40-48),$$

and those for Ca^{42}, Ca^{44}, and Ti^{48} minimize just the χ^2 of the appropriate measured difference. The fit achieved with these experimental results is illustrated in Figs. 6, 8, and 9. The differential cross sections for Ca^{40} and Ca^{48} shown in Fig. 6, and the Ca^{40}-Ca^{48} difference in Fig. 9, include for comparison the fits obtained to the 500-MeV experiments, as described in Sec. XII.

The charge distributions $\rho(r)$ determined by the fitting procedure, which may be reproduced by inserting into Eq. (2) the parameter values given in Table III, are illustrated, for Ca^{40}, Ca^{48}, and Ti^{48}, in Fig. 10.

TABLE III. Numerical values of the parameters for the parabolic Fermi shape [Eq. (2) of Sec. VI], and related quantities. All except w (which is dimensionless) are in F. The errors on these experimentally determined values are discussed in Sec. IX. As is described there, isotopic differences of parameters are known to greater accuracy than individual entries. The values are given here to greater significance than experimental error warrants, to allow accurate reproduction of results given in the text, and to permit easy examination of parameter isotopic differences. $\langle r^2\rangle^{\frac{1}{2}}$ is the rms radius, and $r_{0.5}$ and t are the numerically determined half-value radius and (90–10%) skin thickness, respectively (see Sec. IX). The first five rows come from the main experimental results, at 250 MeV, as described in Sec. VI. The sixth is the separate best fit to the Ca^{40} absolute cross section alone, and the seventh is the subsequent best fit to the Ca^{40}-Ca^{48} difference. The eighth and ninth rows are a mutual best fit to the 500-MeV electron scattering and to the muonic x-ray $K\alpha_1$ Ca^{40}-Ca^{48} energy difference (Sec. XIII). (The actual energy used in the calculation in each case is 0.5 MeV less than the beam energy, to allow for energy loss in the target.) The tenth row is the Fermi shape ($w=0$).[a]

Nucleus	c (F)	z (F)	w	$r_{0.5}$ (F)	$r_{0.5}/A^{\frac{1}{3}}$ (F)	t(90–10%) (F)	$\langle r^2\rangle^{\frac{1}{2}}$ (F)
Ca^{40}	3.6758	0.5851	−0.1017	3.5548	1.0394	2.681	3.4869
Ca^{42}	3.7278	0.5911	−0.1158	3.5876	1.0321	2.724	3.5166
Ca^{44}	3.7481	0.5715	−0.0948	3.6374	1.0303	2.630	3.5149
Ca^{48}	3.7444	0.5255	−0.03	3.7133	1.0218	2.351	3.4762
Ti^{48}	3.8551	0.5626	−0.0761	3.7680	1.0368	2.580	3.5844
Ca^{40}(250′)	3.725	0.591	−0.169	3.516	1.028	2.77	3.452
Ca^{48}(250′)	3.918	0.521	−0.124	3.682	1.013	2.48	3.444
Ca^{40}(500)	3.697	0.587	−0.083	3.599	1.052	2.67	3.526
Ca^{48}(500)	3.797	0.534	−0.048	3.746	1.031	2.42	3.517
Ca^{40} [a]	3.602	0.576	0	3.604	1.054	2.51	3.52

[a] Obtained in Ref. 3.

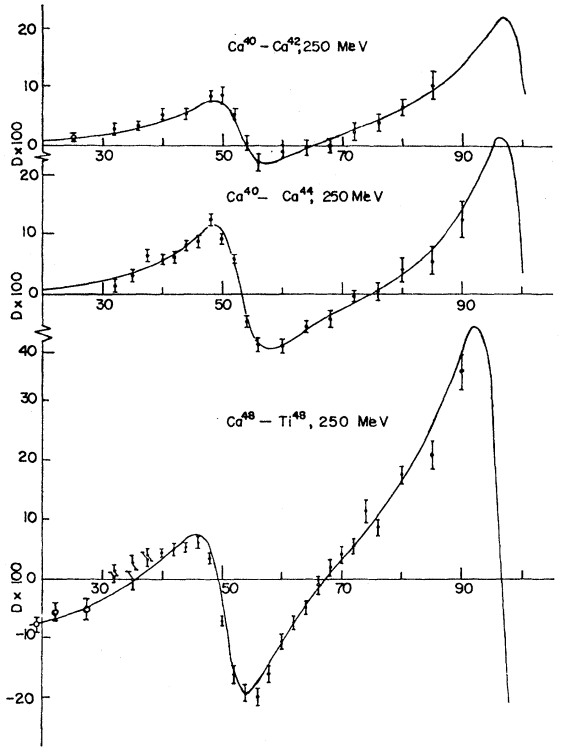

FIG. 8. Comparison of experimental and calculated values of $D(\theta)$ for scattering at 250 MeV versus scattering angle. For each pair of nuclei, e.g., Ca^{40}-Ca^{42}, the quantity plotted is $D(\theta)=[\sigma_{40}(\theta)-\sigma_{42}(\theta)]/[\sigma_{40}(\theta)+\sigma_{42}(\theta)]$. The incident energy used is 249.5 MeV (see caption to Fig. 6) and the parameter values for the calculations are those of Table III. The Ca^{48}-Ti^{48} results include points taken at $\theta=32°$ and 150, 175, and 200 MeV, here plotted at 19.0°, 22.0°, and 27.5°, and the Ca^{40}-Ca^{42} results a point taken at $\theta=36°$, and 175 MeV, here plotted at 25.0°, as is justified in Sec. XIII.

This figure gives also $4\pi r^2\rho(r)$, a quantity which, as is discussed in Sec. X, the phenomenological analysis determines better than $\rho(r)$. It is evident that the charge distributions for these isotopes are all very similar in over-all behavior. It is a consequence of the greater accuracy of the isotopic difference measurements, however, that the small differences among the charge distributions of Fig. 10 are determined more accurately than the individual shapes. It is thus appropriate to emphasize what in Fig. 10 appear as small isotopic differences among the charge distributions, and to concentrate attention on the differences $\Delta\rho(r)$, and $4\pi r^2\Delta\rho(r)$, for various pairs of nuclei. To the fits to experiment shown in Figs. 8 and 9, Figs. 11 and 12 give the corresponding charge distribution differences. The significance of their dependence on r is discussed in Sec. XIV.

Because of various experimental errors, there are uncertainties in the parameters listed in Table III and consequently in the charge distributions plotted in Figs. 10–12. The errors on differential cross sections and on the quantity D listed in Table II provide one source. Because of the relative magnitude of these errors, it will be clear that the rms deviations of isotopic differences of parameters are considerably smaller than the deviations of the parameters themselves. The other source of uncertainty in the isotopic differences is the target-thickness uncertainty of $\pm 1\%$. For the Ca^{40}-Ca^{48} difference, the rms deviations for Δc, Δz, and Δw from the former source are respectively 0.005 F, 0.0013 F, 0.0048, and their variations from the latter source are 0.012 F, 0.005 F, 0.0081. The deviations are strongly correlated, as can be understood from remarks made in Sec. VIII, so that the resulting uncertainty in $\Delta\rho(r)$ is smaller than would be produced by allowing one of the parameter differences to vary independently of the others. These uncertainties are illustrated in Fig. 13. It is seen that even from the target-thickness uncertainty, the major source, the main features of $\Delta\rho(r)$ are not qualitatively affected by these errors.

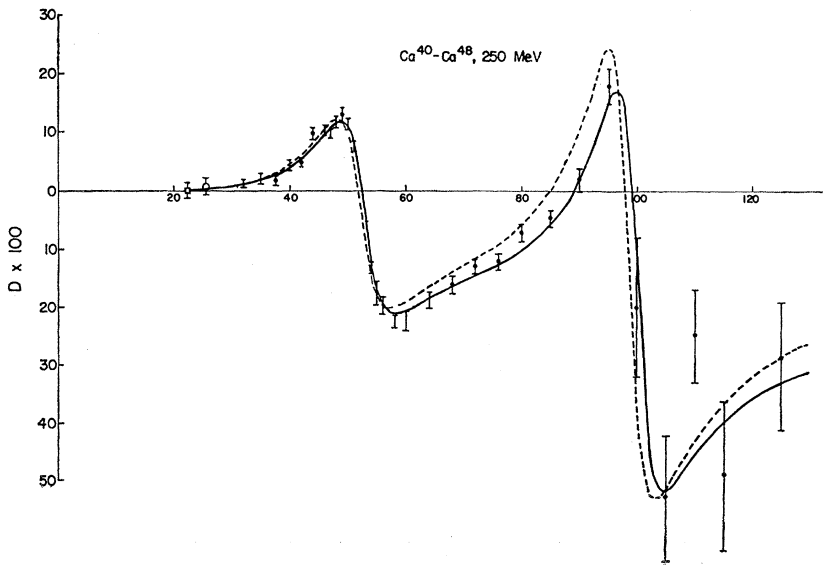

FIG. 9. As for Fig. 8, for the isotopic difference Ca^{40}-Ca^{48}. Points taken at 175 and 200 MeV are here plotted at 22.2° and 25.5°, as is justified in Sec. XIII. The dashed curve comes from the 500-MeV analysis, as described in Sec. XII.

Other entries in Table III give Ca^{40} results obtained by slightly different procedures. Those on the sixth row come from minimizing $\chi^2(40)$ alone. From that procedure, the rms deviations of c, z, and w are 0.015 F, 0.0040 F, and 0.018. [The Ca^{48} parameters obtained by subsequently minimizing $\chi^2(40-48)$ are given in the seventh row.] Those on the eighth row are from the 500-MeV experiments, obtained in a manner described in Sec. XII. The variations in parameter values among these three entries for Ca^{40} are larger than the rms deviations of row 1 but are compatible with them, allowing for the strong correlations. They represent an uncertainty in the parameter values of any one of the shapes quoted in Table III, taken individually (but not an uncertainty in parameter differences!). Again, the variations are strongly correlated. The charge distributions for the three Ca^{40} shapes are plotted in Fig. 14, together with the Fermi shape ($w=0$) obtained in Ref. 3. The curves are indistinguishable for radii greater than 3 F, the variation being greatest at the origin, as we expect. It seems clear that the value of $\rho(r)$ beyond $r\simeq 3$ F is being determined to some extent uniquely from the various experiments. Thus, for example, $\rho(r=3.5$ F) is known more accurately than the variation of $r_{0.5}$ among the various entries for Ca^{40} in Table III would suggest. One reason for this is that the half-radius $r_{0.5}$ and the 90–10% skin thickness t are defined with respect to the central density. Since that quantity varies among the shapes compared, $r_{0.5}$ and t are thus not the model-independent parameters needed to characterize what is determined best by our experiments. By evaluating one of the newly determined shapes for

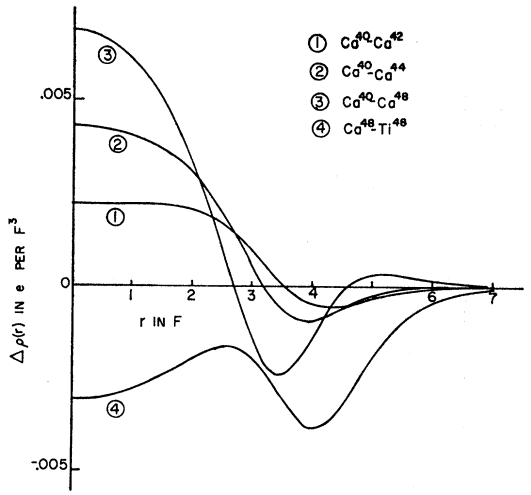

FIG. 11. Charge distribution differences for the measured isotopic pairs indicated, as functions of the radius. These are the results of the phenomenological analysis of the 250-MeV scattering, and are calculated by inserting into the parabolic Fermi shape (2), Sec. VII, the parameter values given in the first five rows of Table III.

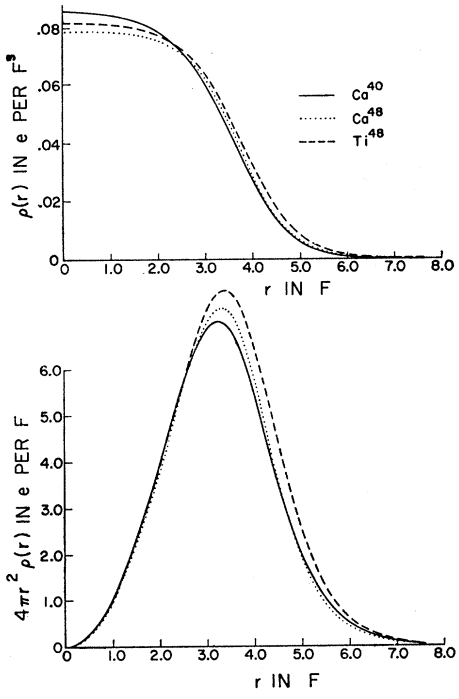

FIG. 10. Charge distributions of Ca^{40}, Ca^{48}, and Ti^{48}, and $4\pi r^2$ times these quantities, obtained in the present analysis. They are parabolic Fermi shapes, Eq. (2), with parameter values taken from rows one, four, and five of Table III.

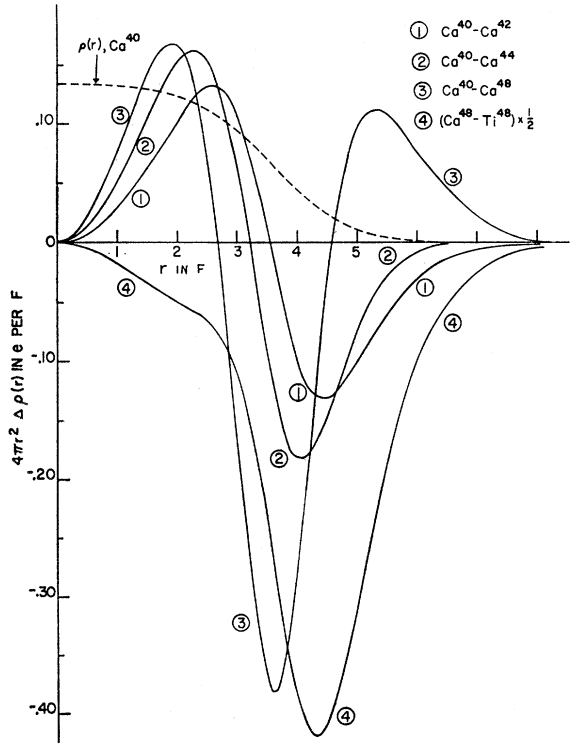

FIG. 12. Charge distribution differences multiplied by $4\pi r^2$ versus r, for the measured isotopic pairs indicated, as is described in the caption to Fig. 11.

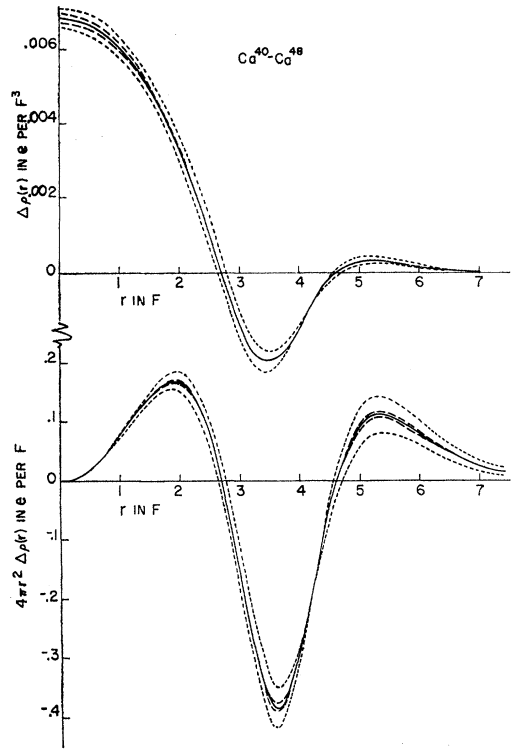

FIG. 13. The Ca^{40}-Ca^{48} charge distribution difference obtained from 250-MeV scattering, and this quantity multiplied by $4\pi r^2$, versus r together with variations allowed because of some of the experimental errors. The inner pair of dashed curves represents uncertainty due to the errors given in Table IIa, and the outer pair of dotted curves that arising from the 1% target-thickness uncertainty.

Ca^{40}, preferably from the first entry in Table III, it is possible to reproduce that part of $\rho(r)$ which seems to be common to all of our shapes. In Fig. 15, the Ca^{40}-Ca^{48} charge distribution differences corresponding to rows 6 and 7 of Table III, with the alternative fitting procedure for the 250-MeV results, and those corresponding to rows 8 and 9, coming from the 500-MeV results, are compared with our main 250-MeV result. The agreement here, and in the parameter differences Δc, etc., is closer than that among the individual Ca^{40} shapes, as is expected from the experimental data and our fitting procedure.

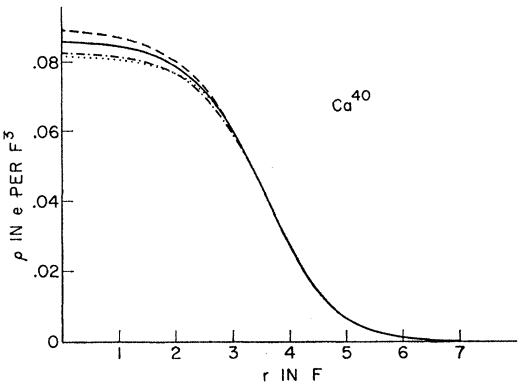

FIG. 14. Charge distributions for Ca^{40}, corresponding to parameter sets given in Table III. The full curve, row 1 of Table III, is from the complete analysis of the 250-MeV data. The dashed curve, row 6, is from the Ca^{40} cross section alone. The dash-dot curve, row 8, is from the 500-MeV data. The dotted curve, row 10, is the Fermi shape obtained in Ref. 3.

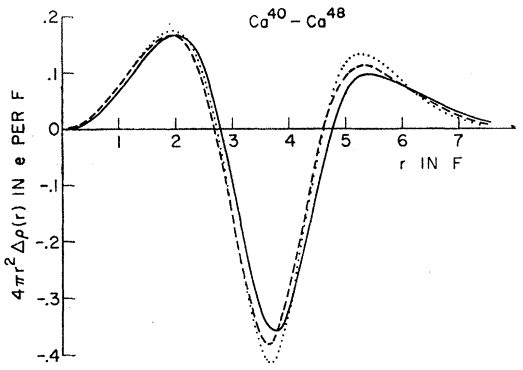

FIG. 15. Comparison of the Ca^{40}-Ca^{48} charge distribution differences obtained with the 500-MeV analysis (full curve) and the main 250-MeV result (dashed curve). The dotted curve, from rows 6 and 7 of Table III, comes from a different, poorer treatment of the 250-MeV data (see Sec. IX).

The length parameters in Table III are also affected by the 0.5% uncertainty in the value of the incident energy. This produces in a very direct way a 0.5% additional uncertainty in c and z for all shapes. The effect on isotopic differences is negligible, but on the muonic x-ray energy it is the largest source of error.

There is a completely different source of uncertainty in $\rho(r)$, arising from the finite range of recoil momentum explored, and having implications as regards the particular choice of shape (2) in Sec. VII. This is discussed in the following section.

X. CHARGE DISTRIBUTION UNCERTAINTIES

To justify the suitability of Eq. (2) as a general shape to be used in determining phenomenological charge distributions, we can illustrate the convergence of successive choices of shape. The present results with the parabolic Fermi shape are compared in Figs. 16 and 17 with earlier fits using the Fermi shape ($w=0$) and the modified Gaussian shape:

$$\rho_{MG}(r)=\rho_0\{\exp[(r^2-c^2)/z^2]+1\}^{-1}. \quad (3)$$

For the difference Ca^{40}-Ca^{48}, Fig. 17, it is very suggestive that our present results are an improvement over the earlier ones, and the χ^2 values (given in the caption) substantiate this. For the Ca^{40}-Ca^{48} difference, Fig. 16, where the data do not cover the second diffraction maximum, the variation among all three shapes is very small. One sees that including nonzero values of w improves the fit where necessary, and in any case does no damage.

We believe that if the shape chosen is sufficiently

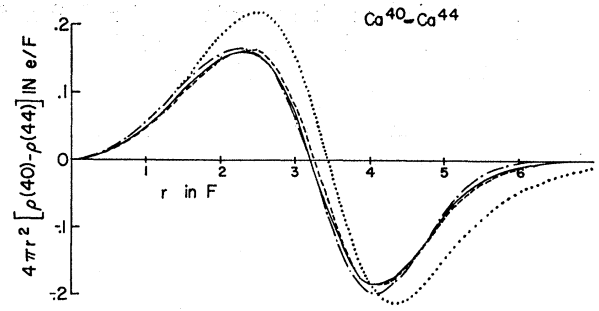

FIG. 16. Plots of the charge distribution isotopic difference Ca^{40}-Ca^{44}, multiplied by $4\pi r^2$, versus r. They illustrate the effect of using successively more flexible analytic expressions for $\rho(r)$. The case of a Fermi distribution [Eq. (2) with $w=0$] in which Δz, the skin-thickness difference, is held at zero, is shown as a dotted line. The dashed curve is for a Fermi distribution without this constraint, the dash-dot curve is for a modified Gaussian shape, Eq. (3), and the full curve represents our present results with the parabolic Fermi shape, Eq. (2), and all parameters allowed to vary. For the last three cases, the values of χ^2 are, respectively, 31.1, 27.5, and 16.6 (20 data points).

flexible, the exact functional choice is not crucially important. Parameters may be introduced in different ways, but the values they take will accommodate to the functional difference so as to yield a common charge distribution. Analyses with different functional forms for $\rho(r)$ are being carried out by us, and preliminary calculations with the Fermi shape generalized in a different way from Eq. (2)[25] reproduce for Ca^{40}-Ca^{48} the results reported here.

An alternative method for examining the uniqueness in the determination of $\rho(r)$ by $d\sigma/d\Omega$ is via Fourier

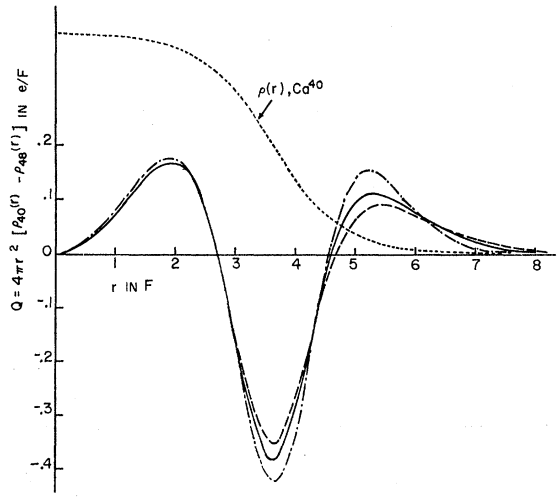

FIG. 17. Charge distribution differences for Ca^{40}-Ca^{48} coming from various analytic expressions for $\rho(r)$ versus r. The curves are shown with the same conventions as the corresponding curves in Fig. 16, omitting the first case. The values of χ^2 are respectively 54.6, 66, and 35.3 (31 data points).

[25] D. G. Ravenhall, B. C. Clark, and R. Herman (unpublished). With $f(r)$ the Fermi shape, Eq. (2) with $w=0$, we have used $\rho(r)=\rho_0 f(r)^n$, where n was taken to be 1.4.

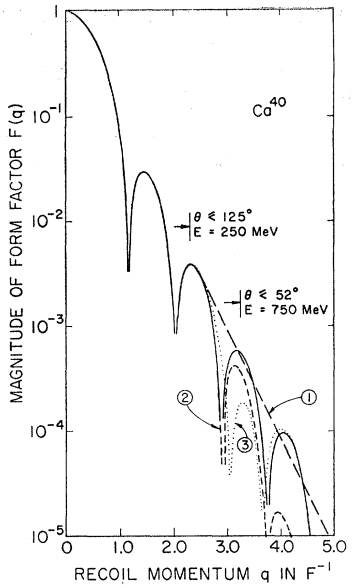

FIG. 18. Form factor (magnitude) for Ca^{40} plotted versus $q=2E_0\sin\frac{1}{2}\theta$, the recoil momentum. At each zero, the form factor changes sign. The full curve, $F_0(q)$ of Sec. X, comes from the charge distribution whose parameters are given in the first row of Table III. The other curves, labeled (1), (2), and (3), assume various forms for $F'(q)$ in the regions of large, unexplored q, as is described in Sec. X.

transforms. It is suggested by the Born approximation, but does not in fact rely on it. An application of the same ideas, in use by us for many years, has been made in the recent analysis of electron-calcium scattering at 750 MeV.[13] The Fourier transform of a typical Ca^{40} charge distribution, $\rho_0(r)$,

$$F_0(q)=\int d^3r\,\rho_0(r)\exp(i\mathbf{q}\cdot\mathbf{r})\Big/\int d^3r\,\rho_0(r)$$

$$=\frac{4\pi}{Ze}\int_0^\infty\frac{\sin qr}{qr}r^2\rho_0(r)dr\,, \tag{4}$$

is a rapidly decreasing, oscillating function, the logarithm of whose magnitude is shown in Fig. 18. Because the Born approximation gives a reasonable qualitative description of the scattering process, it is possible to associate the maxima and minima of $F_0(q)$, i.e., the maxima of $|F_0(q)|$, with the maxima of the differential cross section, q being physically the recoil momentum. The fact that the experimental measurements on Ca^{40} and Ca^{48} at 250 MeV, for example, extend to $\theta=125°$ means that $F_0(q)$ has been measured only for $q\lesssim 2.3$ F^{-1}. The further diffraction structure that the fitted $\rho(r)$ predicts at larger q values is not in fact tested by this experiment.

Measurements at 750 MeV,[13] on Ca^{40} and Ca^{48}, have extended the explored range of q values to ~ 3.2 F^{-1}, and reproduce accurately the diffraction maximum centered at $q\simeq 2.4$ F^{-1}, which the 250-MeV cross

section barely reaches. But for each nucleus, there is a range of recoil momenta q beyond which $F_0(q)$ has not been measured. New form factors $F'(q)$, which are identical with $F_0(q)$ over the measured range but which can differ from $F_0(q)$ in an arbitrary, but reasonable, manner at larger q, are then equally acceptable fits to experiment. The (inverse) Fourier transform of these new functions $F'(q)$ are new charge distributions $\rho'(r)$:

$$\rho'(r)=\frac{Ze}{8\pi^3}\int d^3q\, F'(q)e^{(-iq\cdot r)}$$

$$=\frac{Ze}{2\pi^2}\int_0^\infty \frac{\sin qr}{qr}q^2F'(q)dq. \quad (5)$$

We verify by a partial-wave calculation that, for the cases we discuss, $\rho'(r)$ leads to a differential cross section experimentally indistinguishable from that of $\rho_0(r)$, the original shape, over the measured range of q. The difference $\rho'(r)-\rho_0(r)$ now represents the uncertainty in our knowledge of the charge distribution due to the upper limit on measured recoil momenta q. Of the three cases we consider, the first, (1), assumes that beyond $q=2.5$ F^{-1}, $F_1'(q)$ has about the same exponential decrease as the envelope of $F_0(q)$, but has no oscillations. This is a drastic assumption which the

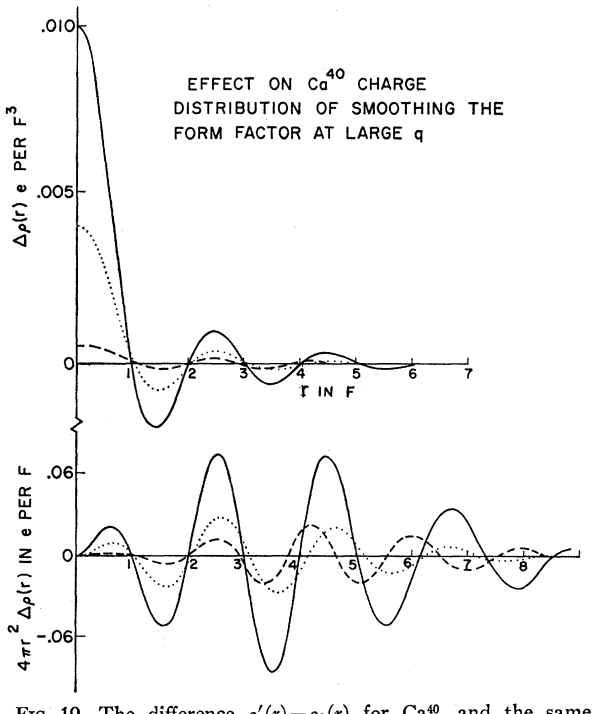

FIG. 19. The difference $\rho'(r)-\rho_0(r)$ for Ca^{40}, and the same quantity multiplied by $4\pi r^2$, versus r. As is described in Sec. X, this function measures the uncertainty in the deduced charge distribution due to the upper limit on explored recoil momenta q. The three cases (1), full line, and (2), and (3), drawn with the same conventions as the corresponding curves in Fig. 18, show the extent to which uncertainty is reduced as that upper limit is increased.

750-MeV experiments already rule out for Ca^{40} and Ca^{48}, but it is in principle a tenable possibility for the other nuclei. The quantity $\rho_1'(r)-\rho_0(r)$, and also this function multiplied by $4\pi r^2$, is shown in Fig. 19. The implied uncertainty is very large at $r=0$, but its over-all magnitude is less than a half of the observed isotopic differences, discussed later in Sec. XIII. This is still disturbingly large. As we have noted, however, the 750-MeV scattering results show that, at least for Ca^{40} and Ca^{48}, $F_0(q)$ is known better than $F_1'(q)$ assumes. A more reasonable assumption, case (2), is that beyond $q=2.5$ F^{-1}, $F_2'(q)$ still oscillates, but with an amplitude which decreases compared with $F_0(q)$. Specifically, for $q>2.5$ F,

$$F_2'(q)=F_0(q)\exp[-(q-2.5)^2/1.28].$$

This is shown as (2) in Fig. 18, and the effect on the charge distribution is given in Fig. 19. The implied uncertainty in $\rho_0(r)$ is reduced considerably from case (1), although at large r it is large enough for $\rho_2'(r)$ to be negative in some regions. Avoiding that situation puts a further constraint on the large q variation. In over-all behavior, the uncertainty implied by case (2) is sufficiently small that its presence would not change qualitatively any of the conclusions to be drawn from the charge distribution isotopic differences. The third case (3), also illustrated in Figs. 18 and 19, represents the analysis of the measured cross sections for Ca^{40} at 750 MeV.[13] The departure of $F_3'(q)$ from $F_0(q)$ in the region around $q=3$ F^{-1} is now not an uncertainty, but a real observed effect. The ripple required in the charge distribution is small enough as not to change any of the conclusions we draw in the present work. Because of the upper limit $q=3.2$ F^{-1} on observed recoil momenta, it also has an uncertainty which may be explored in the above manner. Our conclusion so far as the present work is concerned is that, while in principle the finite extent of explored recoil momenta introduces a rather large uncertainty in the deduced isotopic charge differences, other experiments confirm, for Ca^{40} and Ca^{48}, and lead us to hope, for the other nuclei, that the actual uncertainty is small enough as to not affect them in any important way.

Inaccuracies in the cross section over the measured range of q can be treated in a similar way, of course. That $r^2\rho(r)$ is affected less than $\rho(r)$ is understood from the occurrence in the Fourier transform integrals of $r^2\rho(r)$ and $q^2F(q)$, rather than $\rho(r)$ and $F(q)$. It, and our general experience, leads us to believe that $r^2\rho(r)$ is a property of the nuclear charge density that our experiments determine better than $\rho(r)$ itself. We use this fact in our discussion of the results of the analysis.

XI. COMPARISON WITH MUONIC X-RAY EXPERIMENTS

For nuclei in the calcium region, the muonic x ray from the $2p\rightarrow 1s$ transition tests sensitively the over-all

size of the charge distribution. The rms radius, which is to a good approximation the parameter determined for this region of nuclei, is not measured directly in our electron scattering experiments, since we do not make a detailed exploration at low momentum transfer. One approach to the determination of a phenomenological charge distribution is thus to fit to all experiments, electron scattering, and muonic x rays. In Sec. XII we use this approach for our 500-MeV data, since at that energy no cross sections were obtained at recoil momenta below the first diffraction dip.[26]

It is to be remembered, however, that nuclear polarization modifies the muonic atom problem, as well as the electron scattering problem, although it would be expected to contribute less than about 0.2 keV to the $2p \rightarrow 1s$ energy, and presumably a lesser amount to the isotopic difference in energy. Our 250-MeV analysis has been made without reference to muon data, since only after the bulk of our analysis was completed have there appeared remarkably precise new muon results.[8] The muon transition energies and isotopic energy differences predicted from electron scattering at 250 MeV can therefore be compared with the muon measurements to examine any possible discrepancies.

The method used for computation of muonic energy levels has been described earlier,[3] and is fairly standard. The vacuum polarization potential, to lowest order in α, is included with the Coulomb potential in the Dirac equation. Uncertainties due to computational techniques are eliminated by the use of double-precision arithmetic. Those due to the error level of the fundamental constants and of higher radiation corrections are small enough to be ignored in the present comparison. In Table IV we compare the results in the form of muon transition energies so as to avoid the slight model dependence that occurs with mean-square radii. (Values of the latter quantities are given in Table III.) The errors quoted on the isotopic differences come partly from statistics, but mainly from the target-thickness uncertainty of $\pm 1\%$. The error on the Ca^{40} x-ray energy itself comes mainly from the $\pm 0.5\%$ uncertainty in energy of the incident electron. That part which comes from the spread in parameter values of the 250-MeV Ca^{40} results in Table III is smaller than would be estimated from the spread in $\langle r^2 \rangle^{1/2}$, the rms radius. (The mesic x-ray energy depends to an appreciable extent here on the shape, i.e., on all of the parameters c, z and w, and not just on $\langle r^2 \rangle^{1/2}$.) The remarkable agreement in energy difference between muonic x-ray experiment and the electron scattering predictions is a very useful check of both methods, and sets a limit on effects such as nuclear polarization not included in either analysis (to the extent that it would affect them differently, of course). It may also indicate that our estimates of target-thickness and incident-energy uncertainties were a little pessimistic.

[26] In more recent data, such information has become available.

TABLE IV. Comparison of muonic x-ray energies and energy differences for the $K\alpha_1 (2p_{\frac{3}{2}} \rightarrow 1s_{\frac{1}{2}})$ transition given by the charge distributions obtained from our 250-MeV analysis, the first five rows of Table III, with the experimental results of Ehrlich *et al.*[a] (see Sec. XI).

Nuclei	$\Delta E(K\alpha_1)$ in keV: Electron scattering	$\Delta E(K\alpha_1)$ in keV: x-ray experiment
Ca^{40}-Ca^{42}	0.82±0.40	0.69±0.06
Ca^{40}-Ca^{44}	0.61±0.37	0.89±0.05
Ca^{40}-Ca^{48}	−0.54±0.35	−0.47±0.12
Ca^{40}	783.8 ±2	784.05±0.16

[a] Reference 8.

As an exercise, and to illustrate the high precision of both experiments, we can set an upper limit on the size difference of the electron and the muon, provided we assume for the moment that such a difference is the only source of a discrepancy. We have assumed that the electron has zero "size," and have then predicted the muonic x-ray energy to about ±2 keV.[27] This, compared with 200 keV, the nuclear size effect in calcium, is 1 part in 100. If the muon had a finite rms radius r_μ, the relative effect on the transition energy would be $(r_\mu/r_N)^2$. Inserting the rms nuclear radius value $r_N \simeq 3.5$ F, we obtain the result $r_\mu \lesssim 0.35$ F. This compares well with other measurements of the muon size[28]: from muon-proton scattering, $r_\mu \lesssim 0.25$ F; from the muon anomalous moment, $r_\mu \lesssim 0.15$ F.

XII. EXPERIMENTS AT 500 MeV

As can be seen in Figs. 20 and 21, the Ca^{40} and Ca^{48} measurements at 500 MeV start at $\theta = 32°$ and do not cover the region of small momentum transfer before the first diffraction dip. It is possible to make a fit to these data, but the resulting Ca^{48} charge density has an rms radius which differs very significantly from that obtained at 250 MeV, and we believe this is because there are no experimental data at angles so small that the cross sections determine the rms radius.[26] To include a constraint on the over-all radius, and still make an analysis independent of the 250-MeV results, terms have been included in the expression for χ^2 which favor, according to the experimental errors, shapes for which the muonic x-ray transition energies ($K\alpha_1$) and energy differences are in agreement with the measured values. The 500-MeV parameter values quoted in Table III come from this fit. As can be seen in Fig. 15, the shapes obtained at 500 MeV by this means are in good agreement with the 250-MeV results. The comparison serves as a useful check on our methods, but because of our use at 500 MeV of muonic x-ray information, which is a physical different process associated with quite different probe wavelengths, it does not provide

[27] This error comes mainly from the 0.5% uncertainty in incident energy. In presently taken data this is reduced considerably.

[28] Results summarized in the review paper of W. K. H. Panofky, International Conference on Elementary Particles, Heidelberg, Germany, 1967 (unpublished).

a sound basis for a detailed examination of energy dependence in the electron-scattering process.

XIII. ROOT-MEAN-SQUARE RADII

Of the two other methods for determining charge radii which we can compare with, that of muonic x rays has been discussed in another section. The other method is really the same as ours, fundamentally: electron scattering at lower energies. Experiments at Darmstadt[29] use electron energies of up to 60 MeV, and the resulting cross sections, involving only small recoil momenta, depend mainly on the rms radius of the charge density. Even there, however, there is a certain amount of "model dependence," i.e., the cross sections really depend a little on the separate $r_{0.5}$ and t parameters. In other words, at recoil momenta where finite size produces a usefully measurable decrease in the Coulomb cross section, the wavelength associated with q is small enough to explore more detailed structure than just $\langle r^2\rangle$. The results of the Darmstadt group include all information necessary to allow for this model dependence. Their result for Ti^{48}, when we assume a t value about equal to the one we have obtained, is in very close agreement with ours:

$$\langle r^2\rangle_{Ti}^{1/2}=3.569\pm0.04\text{ F}\quad\text{(Darmstadt[29])},$$
$$=3.584\pm0.04\text{ F}\quad\text{(present work)}.$$

The consistency of the points taken at 150 MeV for Ca^{48}-Ti^{48}, and at 175 and 200 MeV for Ca^{40}-Ca^{48}, with the main body of 250-MeV results confirms our confidence in the rms radius deduced from our parameters c, z, and w. The validity of our presentation of these data on the 250-MeV graphs, in Figs. 8 and 9, at angles which preserve the correct recoil momentum $q=2E\sin\frac{1}{2}\theta$, has been justified by partial-wave calculations. We verified that for charge distributions of the kind used here, the quantity D depends, to about 0.02%, only on q and not on E and θ separately. The lower-energy data can thus be used to fix D at smaller angles than could be measured at 250 MeV. At such angles D depends mainly on the rms radius difference.

It is to be emphasized that, after the careful analyses associated with the various experiments, the three types of experiment, high-energy electron scattering, low-energy electron scattering, and muonic x rays, agree amazingly well. The well-determined rms radii of all of the isotopes studied must be considered as an unavoidable constraint on any discussion of charge structure of these nuclei. Any suggestion of discrepancies in other regions of the periodic table should be accompanied by an explanation as to why in the Ca-Ti region the discrepancies disappear.

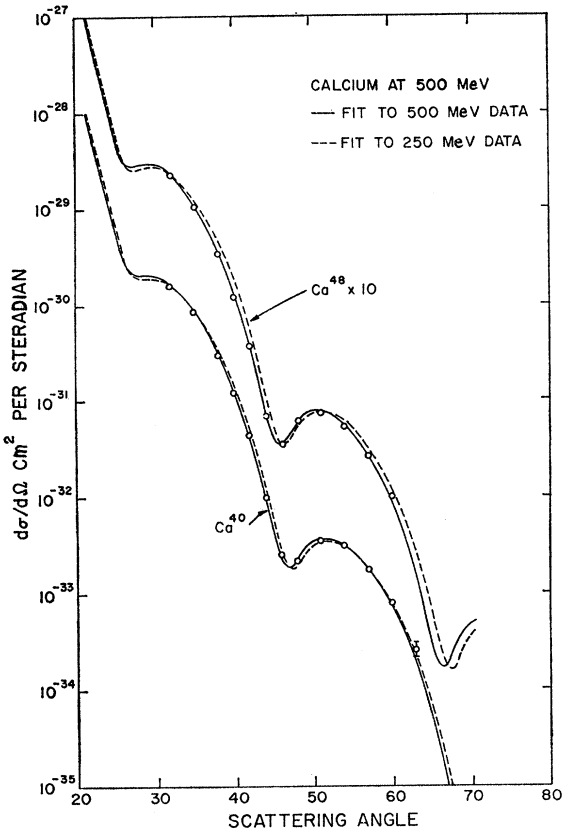

FIG. 20. Differential cross sections for scattering of 500-MeV electrons by Ca^{40} and Ca^{48}. Because of a 0.5-MeV average energy loss in the target, the incident energy used in the calculation is 499.5 MeV. The experimental points are given in Table IIc. The full curves are fits to this data and to muonic x-ray energies, as is described in Sec. XII, and the dashed curve comes from the 250-MeV analysis.

[29] R. Engfer, H. Theissen, and G. J. C. van Niftrik, Proceedings of the International Conference on Electromagnetic Sizes of Nuclei, Carleton University, Ottawa, 1967 (unpublished).

XIV. DISCUSSION

The charge distribution parameter values for all of the isotopes are given in Table III, and some isotopic differences are displayed as percentages of the appropriate Ca^{40} value in Table V. These tables include values of the half-radius $r_{0.5}$, the 90–10% skin thickness t, and the rms radius $\langle r^2\rangle^{1/2}$. Because of the presence in the parabolic Fermi shape (2) of the parameter w, these parameters are not simply related to c and z, and must be calculated numerically. (We note that, especially in comparing isotopic differences, results with this numerical t are noticeably different from what would be obtained by using the familiar formula $t=4.4z$, an approximation for the case $w=0$.)

These tables contain three separate entries for Ca^{40}, Ca^{48}, and the Ca^{40}-Ca^{48} difference, whose origins have been given in Sec. IX. We observe that among the three Ca^{40} entries, the variations in $r_{0.5}$, t, and $\langle r^2\rangle^{1/2}$ are not smaller than the variations in c and z, although the different values taken by w in the three cases clearly have an effect. Figure 14 reveals, however, that for $r\gtrsim3$ F the three charge distributions are much more similar than are the three values of any of the

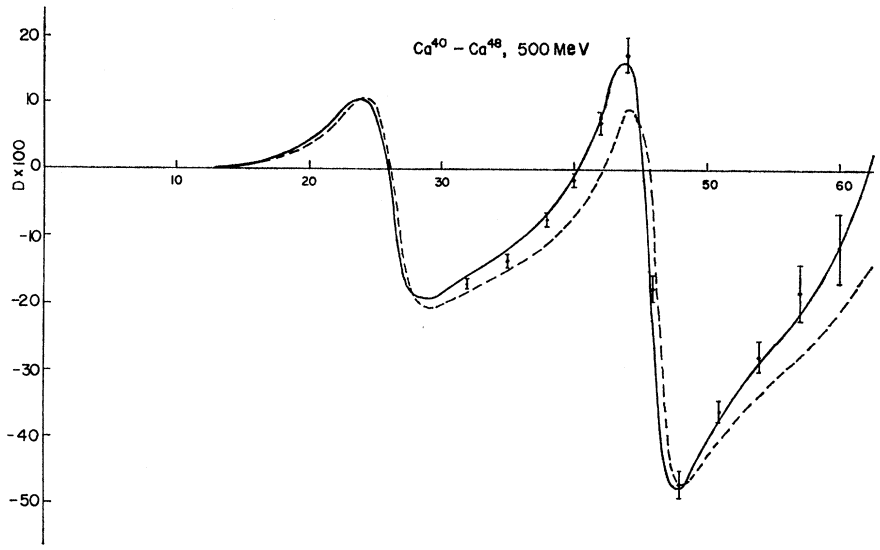

FIG. 21. Comparison of experimental and calculated isotopic difference D for Ca^{40}-Ca^{48}, at 500 MeV, as is described in the caption to Fig. 20.

parameters we quote. It may be possible to define more appropriate, i.e., less variable, parameters than $r_{0.5}$, t, and $\langle r^2\rangle^{1/2}$, although we have preferred to make our discussion in terms of the charge distributions themselves. As regards the three entries for the Ca^{40}-Ca^{48} difference in Table V, and the corresponding curves of $4\pi r^2\Delta\rho(r)$ shown in Fig. 15, it is to be emphasized how similar are both the parameter differences and $\Delta\rho$ for these three cases. These results justify our belief that the experimental measurement of D, Eq. (1), yields a $\Delta\rho(r)$ and parameter differences which are relatively independent of the precise form chosen for the Ca^{40} shape.

The first five rows of Table III, and the corresponding entries in Table V, contain the charge distribution parameter values of our main 250-MeV analysis. The large isotopic variation in t is associated with the fact that the A dependences of $r_{0.5}$ and $\langle r^2\rangle^{1/2}$ are quite different. For the Ti^{48}-Ca^{48} difference, $r_{0.5}$ increases almost like $A^{1/3}$, while $\langle r^2\rangle^{1/2}$ increases by less than half this amount. For the four calcium isotopes, $r_{0.5}$ increases steadily, and by somewhat more than a half of the amount expected from an $A^{1/3}$ dependence. The variation of $\langle r^2\rangle^{1/2}$ is quite irregular, however. A measurement of $\Delta\langle r^2\rangle^{1/2}$ alone, for the Ca^{40}-Ca^{48} difference, would suggest that, so far as charge distributions are concerned, Ca^{48} was smaller than Ca^{40}. The more detailed electron-scattering results reveal that the situation is more complicated than this. It is thus possibly misleading to draw conclusions about nuclear structure from measurements of the isotopic variation of $\langle r^2\rangle^{1/2}$ alone. (Nevertheless, the accurate measurement of $\Delta\langle r^2\rangle$ provided, e.g., by muonic x-ray measurements,[8] will be a valuable datum to add to electron-scattering studies of charge distributions.)

Since none of the derived parameters we use have any fundamental basis, and since some features of $\rho(r)$ seem to be better determined than the parameters themselves, we now concentrate our discussion on charge distributions as functions of radius. The charge distribution differences corresponding to the parameter values given in Table III have been illustrated in Figs. 11 and 12. The area under the Ca^{48}-Ti^{48} curve (scaled down by a factor $\frac{1}{4}$) represents two units of charge, and provides a criterion for the magnitude of the shifts in charge density observed in other cases. Thus, comparing Ca^{40} and Ca^{48}, about 0.4 proton charges are moved from the center and the extreme tail towards the middle of the surface.

The charge distribution differences, and also their values multiplied by $4\pi r^2$, plotted in Figs. 22 and 23, are combinations of the measured differences, designed

TABLE V. Parameter differences of the entries in Table III, as percentages of the appropriate Ca^{40} values.

Isotopic difference	$\frac{\Delta c}{c_{40}}$	$\frac{\Delta z}{z_{40}}$	Δw	$\frac{\Delta r_{0.5}}{r_{0.5,40}}$	$\frac{\Delta t}{t_{40}}$	$\frac{\Delta\langle r^2\rangle^{\frac{1}{2}}}{\langle r^2\rangle_{40}^{\frac{1}{2}}}$	$\frac{\Delta A^{\frac{1}{3}}}{40^{\frac{1}{3}}}$
Ca^{42}-Ca^{40}	1.41	1.03	−0.0141	0.92	1.64	0.85	1.64
Ca^{44}-Ca^{40}	1.97	− 2.32	0.0069	2.32	− 1.90	0.80	3.23
Ca^{48}-Ca^{40}	1.87	−10.19	0.0717	4.46	−12.28	−0.31	6.27
(Ca^{48}-Ca^{40}, 250′)	2.5	−11.9	0.045	4.7	−10.4	−0.3	6.27
(Ca^{48}-Ca^{40}, 500)	2.7	− 9.0	0.035	4.1	− 9.5	−0.3	6.27
Ti^{48}-Ca^{40}	4.88	− 3.84	0.0256	6.00	− 3.77	2.79	6.27

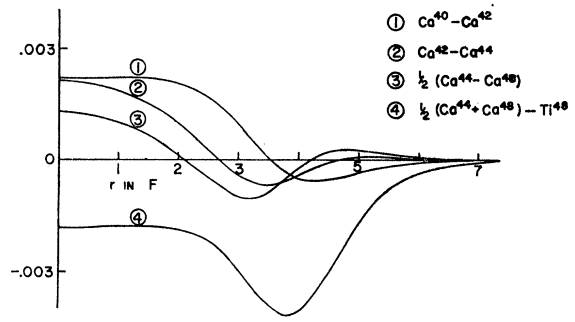

FIG. 22. Charge distribution differences due to the addition of two neutrons as functions of the radius. They are calculated by inserting into the parabolic Fermi shape (2), Sec. XII, the parameter values given in Table III.

to illustrate the changes suffered by the proton distribution as successive neutrons are added. We plot Ca^{40}-Ca^{42}, Ca^{42}-Ca^{44}, and $\frac{1}{2}(Ca^{44}$-$Ca^{48})$, to get as close as we can to the effect of adding two neutrons. We try to isolate the charge distribution of the extra two protons in Ti^{48} by calculating $\frac{1}{2}(Ca^{44}+Ca^{48})$-$Ti^{48}$. This makes the assumption that the unmeasured Ca^{46} charge distribution is approximately $\frac{1}{2}(Ca^{44}+Ca^{48})$. The resulting curves, are of course, completely independent of any nuclear model. [Other combinations are readily obtained by inserting parameters from Table III into the expression for $\rho(r)$.] The two-lobed shape for the Ca^{40}-Ca^{42} difference shown in Fig. 23 represents, in going from Ca^{40} to Ca^{42}, a decrease in central charge density and an increase in charge density at the outside. As can be seen by comparison with the Ca^{40} charge distribution, the nodal point of the difference occurs almost exactly at the midpoint of the Ca^{40} surface. The Ca^{42}-Ca^{44} difference also shows a decrease in central density, but in the outer regions the behavior is qualitatively different. The density at the extreme edge is decreased. The charge moved from the center and the edge is concentrated at the nuclear surface. Similar trends are observed in the $\frac{1}{2}(Ca^{44}$-$Ca^{48})$ difference, the decrease in charge density at the edge being doubled, while the central decrease is halved. The physical picture these changes suggest to us is of a dilatation, and a thinning of the surface of the proton structure of Ca^{40} on adding two neutrons. Further neutrons produce successively less dilatation (the change in central density decreases) and also a tighter structure, with a successively less tenuous edge.

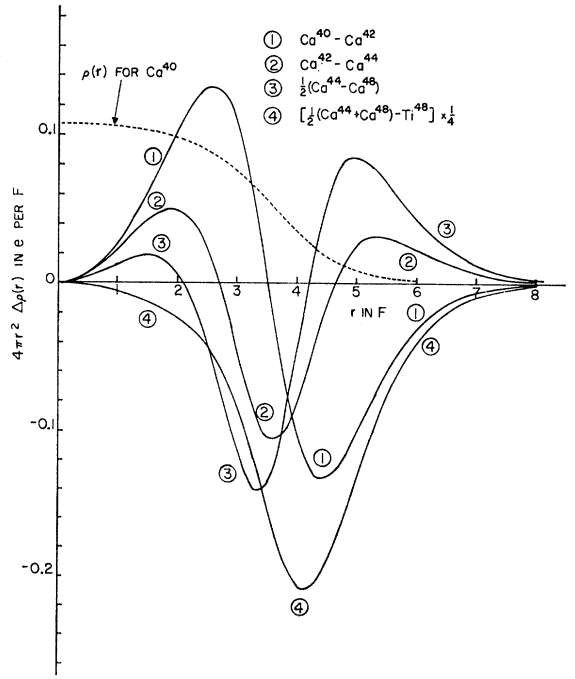

FIG. 23. The charge distribution differences of Fig. 22 multiplied by $4\pi r^2$ as functions of the radius.

The above picture comes directly from experiment, with no injection of information from a detailed model of nuclear structure. To the view of Ca^{40} and Ca^{48} as very stable nuclei, revealed by their energy-level structure and behavior in nuclear reactions, it adds the knowledge that they have tightly bound charge distributions, relative to their neighboring isotopes.

In Fig. 23, the remaining charge distribution difference, multiplied by $4\pi r^2$, $\frac{1}{2}(Ca^{44}+Ca^{48})$-$Ti^{48}$, approximates the spatial distribution of the two protons added to Ca^{46} to make Ti^{48}. It is nodeless, and peaks a little beyond the half-radii of Ca^{48} and Ti^{48}. The added charge density itself (without the factor $4\pi r^2$) is of about the same magnitude at the center as the calcium differences. Any tendency for the added protons to dilate the calcium core would add a positive contribution at small r to the difference as we have defined it. Thus the actual shape observed, with no node, means that the positive contribution from dilatation has been more than cancelled by the charge density of the added protons. Note, however, that this conclusion depends on how well the function coming from $\frac{1}{2}(Ca^{44}+Ca^{48})$ represents the unmeasured charge distribution of Ca^{46}.

XV. NUCLEAR SHELL MODEL

Our results show that the well-known stability of Ca^{40} and Ca^{48}, compared with neighboring nuclei, is exhibited also in their charge distributions. This it perhaps an obvious physical corollary of the nuclear shell model and its placing of Ca^{40} and Ca^{48} as closed-shell nuclei. The model as used to discuss the structure of low-lying levels and the character of nuclear reactions (e.g., pick-up and stripping) does not, however, make any direct prediction of the influence of added neutrons on the filled proton shells. A mechanism for this influence is the virtual excitation, in Ca^{42} for example, of higher proton configurations by the two neutrons, through a residual interaction. There may also occur a variation of the radial wave functions of the single-proton orbitals themselves, due to a dependence on N

and Z of the shell-model potential. The two mechanisms are experimentally indistinguishable, so far as the ground-state wave function is concerned, and in a Hartree-Fock calculation they are to some extent even the same physical process. It is beyond the scope of this paper to pursue this topic further, but comparison of our results with predictions of a Hartree-Fock calculation is very desirable.

A more restricted version of the shell model, with no residual interactions and no population of any but the lowest configurations, has been applied to our experimental results by a number of investigators.[10,11] The nuclear single-particle potential used is of the Woods-Saxon (Fermi) type, with adjustable parameters, and the purpose of the comparisons has been to determine the values of these parameters, and their variation with N, the assumption being made that the single-particle shell model must describe all of the phenomena considered. With varying degrees of ambition, each investigation of this kind has produced a set of parameters—well depth, radius, skin thickness, etc.—which vary rather irregularly with N and A. In the most ambitious of these projects, Swift and Elton[11] attempt to make their model fit the energies of all of the single-proton orbitals, assumed to be known accurately from other experiments. In order to do this they must, of course, take different potential depths for each major shell. Their final result is an interesting parametrization of a large number of data. It is also possible, however, to approach the comparison in a somewhat different way.

The basic question, it seems to us, is how many of our results are described naturally by the single-particle shell model, and which, if any, require the many-body aspects of the model, or even a different model. For example, a natural description of the observed nodeless charge distribution difference $\frac{1}{2}(Ca^{44}+Ca^{48})$-$Ti^{48}$ is that the two protons have gone into the next orbital, $1f_{7/2}$, which has a nodeless radial wave function. Certain features of the Ca^{40}-Ca^{42}, Ca^{42}-Ca^{44}, and $\frac{1}{2}(Ca^{44}$-$Ca^{48})$ differences also arise naturally. The decrease in central density follows from an $A^{1/3}$ dependence of the potential radius. The decrease in density at the extreme edge, in the latter two differences, is qualitatively a consequence of the deeper binding of all the proton orbitals as N increases, as reflected in the increased proton separation energy.[30] Even here, however, a quantitative agreement requires the potential skin thickness between Ca^{40} and Ca^{48} to decrease by 20%, a large variation. We would have expected the skin thickness of the potential, which is due to both protons and neutrons, to change less than the skin thickness of the proton distribution alone. The behavior of the Ca^{40}-Ca^{42} difference at the nuclear edge is even of opposite sign from the subsequent differences. To explain it, one either requires parameter differences of the single-particle model opposite to the subsequent trend, or, more naturally, one invokes an (uncalculated) shell-breaking, many-nucleon effect. In a forthcoming paper,[12] Mather, McKinley, and Ravenhall attempt to approach the comparison with the single-particle shell model with this more qualitative point of view. A fuller discussion and comparison with the previous work is given there.

It is clear from what has been said that the detailed knowledge of the "isotope effect" that electron scattering gives already provides a useful new test of nuclear models. We hope that nuclear theorists will include it in discussions of nuclear models in the future.

ACKNOWLEDGMENTS

We wish to thank the crew of the Stanford Mark III accelerator for their enthusiastic cooperation. Many members of the laboratory contributed directly to the success of this experiment; we would especially like to acknowledge the help of M. Ryneveld and W. Wadensweiler in designing the data-acquisition system.

We wish to thank J. J. Fishman and M. J. Marcotty, General Motors Research Laboratories, for advice and assistance in some parts of the computer programming, and L. R. Mather and R. H. Landau, University of Illinois, for discussions and some calculations.

We also wish to thank Dr. G. L. Rogosa, Atomic Energy Commission, and T. H. Kobisk, Oak Ridge National Laboratory, for their help in obtaining the targets for this experiment.

[30] F. G. Perey and J. P. Schiffer, Phys. Rev. Letters **17**, 324 (1966).